LETTER **Communicated by Rafal Bogacz**

Dynamics of Multiple-Choice Decision Making

Hongzhi You
howardwise@gmail.com
Department of Systems Science and National Key Laboratory of Cognitive Neuroscience and Learning, Beijing Normal University, Beijing 100875, China, and Institute of Neuroinformatics, University of Zurich and ETH Zurich, Zurich 8057, Switzerland

Da-Hui Wang
wangdh.bnu.edu.cn
Department of Systems Science and National Key Laboratory of Cognitive Neuroscience and Learning, Beijing Normal University, Beijing 100875, China

Neuroscientists have carried out comprehensive experiments to reveal the neural mechanisms underlying the perceptual decision making that pervades daily life. These experiments have illuminated salient features of decision making, including probabilistic choice behavior, the ramping activity of decision-related neurons, and the dependence of decision time and accuracy on the difficulty of the task. Spiking network models have reproduced these features and a two-dimensional mean field model has demonstrated that the saddle node structure underlies two-alternative decision making. Here, we reduced a spiking network model to an analytically tractable, partial integro-differential system and characterized not only multiple-choice decision behaviors but also the time course of neural activities underlying decisions, providing a mechanistic explanation for the observations noted in the experiments. First, we observed that a two-bump unstable steady state of the system is responsible for two-choice decision making, similar to the saddle node structure in the two-dimensional mean field model. However, for four-choice decision making, three types of unstable steady states collectively predominate the time course of the evolution from the initial state to the stable states. Second, the time constant of the unstable steady state can explain the fact that four-choice decision making requires a longer time than two-choice decision making. However, the quicker decision, given a stronger motion strength, cannot be explained by the time constant of the unstable steady state. Rather, the decision can be attributed to the projection coefficient of the difference between the initial state and the unstable steady state on the eigenvector corresponding to the largest positive eigenvalue.

1 Introduction

Decision making is the important cognitive process of selecting an option or action among a set of alternatives. Physiological experiments have revealed that decision making involves many brain areas, such as the prefrontal cortex and the parietal cortex (Wang, 2008; Kable & Glimcher, 2009). In discrimination tasks of coherent motion in random dots, neurophysiologists found that the neural activities in monkeys' lateral intraparietal cortexes (LIP) are correlated with neural computation for decision making (Roitman & Shadlen, 2002; Shadlen & Gold, 2004; Churchland, Kiani, & Shadlen, 2008). These LIP neurons selective for a particular saccade display ramp-up activities before the final decision is made. Recently it was also found that the behavioral and neural data in discrimination tasks of coherent motion in random dots are correlated with both motion strength and the number of alternatives. The experimental results showed that these LIP neurons would take longer to accumulate more evidence for more difficult tasks (lower motion strength and more alternatives) and the accuracy of the decision is negatively correlated with the difficulty of the task (Churchland et al., 2008; Bollimunta, Totten, & Ditterich, 2012).

To understand the dynamics of multiple-choice decision making, a number of models have been proposed. For example, a leaky competing accumulator (LCA) model, which considered the leakage of integration and the competitive inhibition between accumulators for different choices, described the process of evidence accumulation and competition observed in the brain and accounted for reaction time distributions in psychophysical experiments (Bogacz, Usher, Zhang, & McClelland, 2007). A model with multiple mutually inhibited leaky integrators that approximated a drift-diffusion process was proposed to explain the behavioral data of multiple-alternative-choice tasks (McMillen & Holmes, 2006). A three-dimensional diffusion model (Niwa & Ditterich, 2008), whose integrators accumulated net sensory evidence for choices, has fitted and predicted the behavioral data.

Although these behavioral data can be fitted by these models, the mechanisms differ in their internal dynamics and therefore make different predictions for neurophysiological data (Ditterich, 2010). Based on the neurophysiological data mentioned above, biophysically plausible spiking network models have been proposed to account for multiple-choice decision tasks. These models, particularly the continuous model by Furman and Wang (2008) and the discrete four-alternative model by Albantakis and Deco (2009), are equipped with strong recurrent excitation and global inhibition and exhibit multiple steady states and a slow dynamic process. Both spiking network models demonstrate typical characteristics in decision-making tasks (Churchland et al., 2008), such as the probabilistic choice in behavior (Wang, 2002; Furman & Wang, 2008), the fact that the earlier stage

plays a more important role in the final choice than later stages (Wong, Huk, Shadlen, & Wang, 2007), the fact that more alternatives slow decision making and decrease the rate of correct choice (Furman & Wang, 2008), and the similarity effects on the choice (Furman & Wang, 2008; Albantakis & Deco, 2009). However, the dynamical mechanisms underlying these characteristics are difficult to uncover using the spiking network models. For two-alternative decision making, theoretical analysis of a firing-rate model reduced from the spiking network model demonstrated that the saddle point underlies decision making and the local dynamics of the saddle point account for the dependence of the reaction time on the coherence level (Wong & Wang, 2006; Wong et al., 2007). For multiple-choice decision making, we can speculate that a similar mathematical structure underlies the decision process and the characteristics of experimental behaviors. In this letter, we applied a mean field approach to construct a partial integro-differential system, which provided a neurodynamical framework to investigate the underlying dynamics of multiple-choice decision making. We used the simplified model to (1) account for the salient observations of the monkey experiments and the spiking network model, (2) reveal different dynamical mechanisms underlying two- and four-choice decision making using the simplified models, and (3) understand the influences of motion strength and choice number on the reaction time.

2 The Model

2.1 The Architecture of the Spiking Network for Multiple-Choice Decision Making. The multiple-alternative decision making in the visual random-dot motion direction discrimination task (see Figure 1A) (Churchland et al., 2008) was simulated using a spiking network (see the top panel of Figure 1B), which reproduced the salient observations in the monkey experiments (Furman & Wang, 2008). This network was originally designed to describe spatial working memory (Compte, Brunel, Goldman-Rakic, & Wang, 2000), and the connectivities between neurons are structured and consistent with a columnar organization in the cerebral cortex (Constantinidis & Steinmetz, 1996; Constantinidis, Franowicz, & Goldman-Rakic, 2001). The pyramidal cells in the network are tuned by their preferred directions and uniformly arranged in a circle. The connections between pyramidal cells are structured as a gaussian function of the difference between their preferred directions: $\omega(\theta' - \theta) = J^- + (J^+ - J^-)\exp(\frac{-(\theta'-\theta)^2}{2\sigma_w^2})$, where θ' and θ are the preferred directions of two pyramidal cells, J^- and J^+ describe the strength of the cross- and iso-directional connections, and the connectivity is normalized as $\int_0^{360} \omega(\theta)d\theta = 360$ (Compte et al., 2000) with $J^+ = 1.73$ and $\sigma_w = 12.76^\circ$. The interneurons are nonselective for direction. The connections to and from the interneurons are uniform: $\omega_{E\leftrightarrow I} = 1$ and $\omega_{I\leftrightarrow I} = 1$.

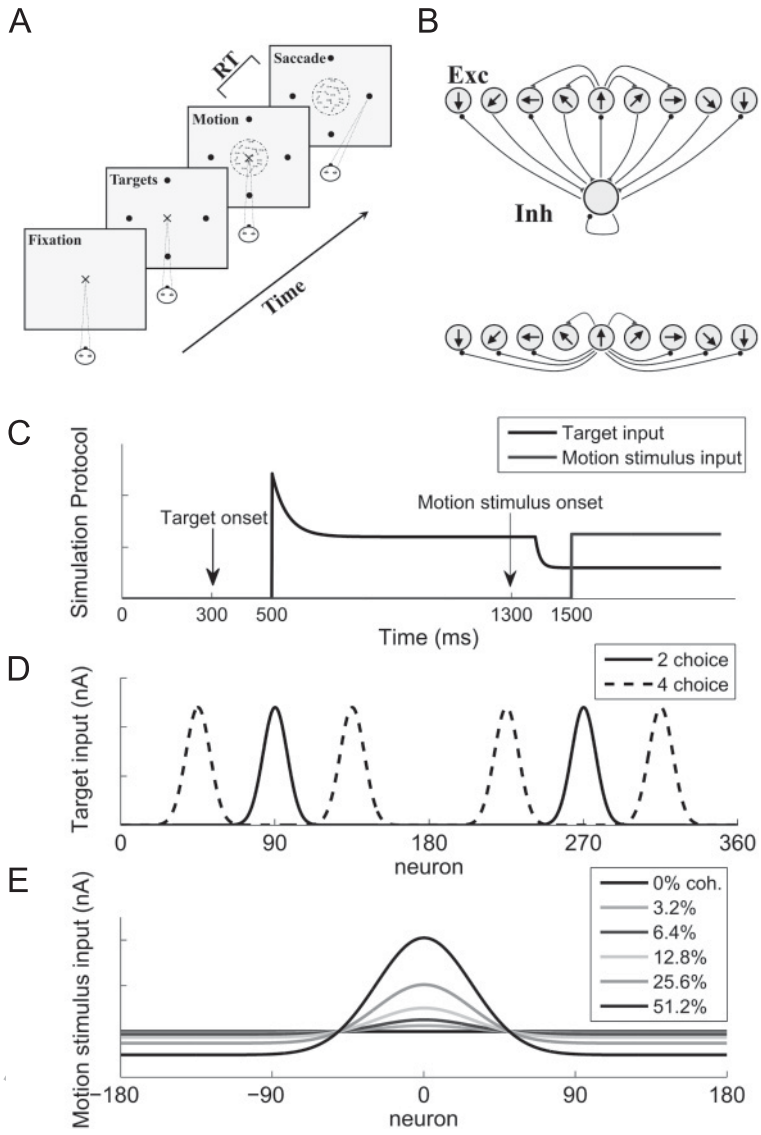

2.2 The Partial Integro-Differential Equation for Multiple-Choice Decision Making

2.2.1 Wilson-Cowan Type Model. Because pyramidal cells are tuned by their preferred directions and interneurons are nonselective for direction (see Figure 1B), the activities of the network can be rewritten as a partial

integro-differential equation following the Wilson-Cowan model (Wilson & Cowan, 1972, 1973):

$$\tau_r \frac{dr_E(\theta,t)}{dt} = -r_E(\theta,t) + \phi[I_{syn,_E}(\theta,t)], \tag{2.1}$$

$$\tau_r \frac{dr_I(t)}{dt} = -r_I(t) + \phi[I_{syn,_I}(t)], \tag{2.2}$$

where $r_E(\theta,t)$ is the instantaneous firing rate of pyramidal cells preferring the direction θ, $r_I(t)$ is the instantaneous firing rate of interneurons, τ_r is the time constant of the population firing rate, and I_{syn} is the total postsynaptic current. The activation function is $\phi(I_{syn}) = \frac{c_{E,I}I_{syn}-I_{E,I}}{1-\exp[-g_{E,I}(c_{E,I}I_{syn}-I_{E,I})]}$ (Abbott & Chance, 2005) with the gain factor of $c_{E,I}$ and the curvature factor of $g_{E,I}$. When $g_{E,I}$ is large, the activation function becomes a linear threshold function with $I_{E,I}/c$ as the threshold current (Wong & Wang, 2006).

2.2.2 Synaptic Currents. Synaptic currents are mediated by the α-amino-3-hydroxy-5-methyl-4-isoxazolepropionic acid receptors (AMPAR), the n-methyl-D-aspartate receptors (NMDAR), and the gamma-aminobutyric

Figure 1: The task and architecture of the network. (A) The multiple-choice decision task used in the experiments. In the task, the monkey is required to fixate on the center of the monitor, and then two or four peripheral targets are presented. After a delay, a patch of dynamic random dots appears, and a fraction of the dots move coherently toward one of the targets, while the remaining dots move randomly. The monkey is required to report the direction of the coherent motion by a saccade to the corresponding targets. (B) Top: Schematic diagram of the spiking network model for multiple-choice decision making. The network consists of excitatory pyramidal cells and inhibitory interneurons. The pyramidal cells are tuned by their preferred directions, which uniformly cover all directions along a circle. The connectivity strength between the pyramidal cells is a gaussian function of the difference between their preferred directions. The interneurons are nonselective, and the connectivity strength to and from the interneurons is uniform (Furman & Wang, 2008). Bottom: Schematic description of the reduced model for decision making. After the reduction, the final reduced model consists of continuous excitatory pools whose preferred directions cover all directions. Because of the gaussian connections between the excitatory pools and strong uniform inhibition, the reduced model has a short-range excitation and long-range inhibition. (C–E) Simulation protocol. (C) Time course of the inputs to the network. (D) Spatial profile of the target inputs to the network. The directions of the targets are 90° and 270° for two choices and 45°, 135°, 225°, and 315° for four choices, respectively. (E) Spatial profile of the motion stimuli with different coherence levels.

acid receptors (GABAR), and their gating variables obey the following dynamics (Wong & Wang, 2006):

$$\frac{dS_{AMPA}(\theta,t)}{dt} = -\frac{S_{AMPA}(\theta,t)}{\tau_{AMPA}} + r_E(\theta,t), \tag{2.3}$$

$$\frac{dS_{NMDA}(\theta,t)}{dt} = -\frac{S_{NMDA}(\theta,t)}{\tau_{NMDA}} + \gamma[1 - S_{NMDA}(\theta,t)]r_E(\theta,t), \tag{2.4}$$

$$\frac{dS_{GABA}(t)}{dt} = -\frac{S_{GABA}(t)}{\tau_{GABA}} + r_I(t). \tag{2.5}$$

AMPARs and NMDARs mediate excitatory postsynaptic currents (EPSC), and GABARs mediate inhibitory postsynaptic currents (IPSC). The neurons also receive external stimuli and background noisy inputs mediated by AMPARs. Therefore, the total synaptic current to pyramidal cells preferring direction θ is

$$\begin{aligned} I_{E,syn}(\theta,t) = {} & I_{AMPA}^{E\to E}(\theta,t) + I_{NMDA}^{E\to E}(\theta,t) + I_{GABA}^{I\to E}(\theta,t) \\ & + I_{AMPA}^{Ext\to E}(\theta,t) + I_{AMPA}^{Back\to E}(\theta,t), \end{aligned} \tag{2.6}$$

where the first three terms are recurrent synaptic currents, $I_{AMPA}^{Ext\to E}(\theta,t)$ is the task-related stimulus mediated by AMPARs, and $I_{AMPA}^{Back\to E}(\theta,t)$ is the background noise current input. These currents are described as

$$I_{AMPA}^{E\to E}(\theta,t) = J_{A,EE}\int_0^{360} \omega(\theta'-\theta)S_{AMPA}(\theta',t)d\theta', \tag{2.7}$$

$$I_{NMDA}^{E\to E}(\theta,t) = J_{N,EE}\int_0^{360} \omega(\theta'-\theta)S_{NMDA}(\theta',t)d\theta', \tag{2.8}$$

$$I_{GABA}^{I\to E}(\theta,t) = J_{G,EI}\omega_{E\leftrightarrow I}S_{GABA}(t), \tag{2.9}$$

where $J_{A,EE}$, $J_{N,EE}$, and $J_{G,EI}$ are the contribution coefficients of the gating variable of AMPARs, NMDARs, and GABARs, respectively, to synaptic currents of the pyramidal cells. Synaptic currents to interneurons are similar to those injecting to pyramidal cells:

$$I_{I,syn}(t) = I_{AMPA}^{E\to I}(t) + I_{NMDA}^{E\to I}(t) + I_{GABA}^{I\to I}(t) + I_{AMPA}^{Ext\to I}(t) + I_{AMPA}^{Back\to I}(t), \tag{2.10}$$

where the first three terms are recurrent currents and described as

$$I_{AMPA}^{E\to I}(t) = J_{A,IE}\int_0^{360}\omega_{E\leftrightarrow I}S_{AMPA}(\theta',t)d\theta', \tag{2.11}$$

$$I_{NMDA}^{E\to I}(t) = J_{N,IE}\int_0^{360}\omega_{E\leftrightarrow I}S_{NMDA}(\theta',t)d\theta', \tag{2.12}$$

$$I_{GABA}^{I\to I}(t) = J_{G,II}\omega_{I\leftrightarrow I}S_{GABA}(t), \tag{2.13}$$

where $J_{A,IE}$, $J_{N,IE}$, and $J_{G,II}$ are the contribution coefficients of the gating variable of AMPARs, NMDARs, and GABARs, respectively, to the synaptic currents of interneurons.

2.2.3 Slow Dynamics of the System. The time constant of the NMDAR's gating variable is much longer than those of AMPARs, GABAR's gating variables, and the firing rates. Therefore, the firing rates, AMPARs, and GABAR's gating variables can be set at their steady states, while the NMDAR's gating variables dominate the dynamic behavior of the system:

$$S_{AMPA}(\theta,t) = \tau_{AMPA}r_E(\theta,t) = \tau_{AMPA}\phi[I_{E,syn}(\theta,t)] \tag{2.14}$$

$$S_{GABA}(t) = \tau_{GABA}r_I(t) = \tau_{GABA}\phi[I_{I,syn}(t)] \tag{2.15}$$

$$\frac{dS_{NMDA}(\theta,t)}{dt} = -\frac{S_{NMDA}(\theta,t)}{\tau_{NMDA}} + \gamma[1-S_{NMDA}(\theta,t)]r_E(\theta,t) \tag{2.16}$$

2.2.4 Ignoring AMPARs. AMPARs mediate fast synaptic currents. An increase in the ratio of AMPAR- to NMDAR-mediated currents decreases reaction time and deteriorates performance. If this ratio is too large, the model cannot account for the experimental results, no matter how finely tuned the parameters are (Wong & Wang, 2006). The slower NMDAR dynamics play a key role in the time integration of decision making. Therefore, the AMPARs can be ignored to simplify the problem and investigate the essential mechanism underlying multiple-choice decision making.

2.2.5 Linearization of the Interneuron's Activation Function. The activation function $\phi(I_{syn}) = \frac{c_I I_{syn} - I_I}{1-\exp[-g_I(c_I I_{syn} - I_I)]}$ is a nonlinear function. However, proper parameters and the input to the interneuron allow us to use a linear function to estimate the activation function of the interneuron (Wong & Wang, 2006):

$$r_I(t) = \phi[I_{I,syn}(t)] \simeq aI_{I,syn}(t) + b. \tag{2.17}$$

By putting formula 2.17 into 2.10 and ignoring the AMPARs, we obtain the recurrent inputs to the interneuron as

$$\begin{aligned} I_{I,syn} &= \int_0^{360} J_{N,IE} S_{NMDA}(\theta)\, d\theta' - J_{G,II}\tau_{GABA} r_I(I_{I,syn}) + I_{AMPA}^{Ext\to I} + I_{AMPA}^{Back\to I} \\ &= \int_0^{360} J_{N,IE} S_{NMDA}(\theta')\, d\theta' - J_{G,II}\tau_{GABA}(aI_{I,syn} + b) + I_{AMPA}^{Ext\to I} + I_{AMPA}^{Back\to I}. \end{aligned}$$

From this equation, we can work out synaptic inputs to the inhibitory pool:

$$I_{I,syn}(t) = \frac{I_{AMPA}^{Ext\to I} + I_{AMPA}^{Back\to I} - bJ_{G,II}\tau_{GABA} + \int_0^{360} J_{N,IE} S_{NMDA}(\theta', t)\, d\theta'}{1 + aJ_{G,II}\tau_{GABA}}. \tag{2.18}$$

Therefore, we obtain inhibitory synaptic currents to the pyramidal cell:

$$\begin{aligned} I_{GABA}^{I\to E}(t) &= J_{G,EI}\omega_{E\leftrightarrow I} S_{GABA}(t) = J_{G,EI}\omega_{E\leftrightarrow I}\tau_{GABA}\phi[I_{I,syn}(t)] \\ &= J_{G,EI}\omega_{E\leftrightarrow I}\tau_{GABA}[aI_{I,syn}(t) + b] \\ &= J_{EIE}\int_0^{360} S_{NMDA}(\theta', t)\, d\theta' + I_R(t), \end{aligned}$$

where $J_{EIE} = \frac{J_{N,IE}J_{G,EI}\omega_{E\leftrightarrow I}\tau_{GABA}}{1+aJ_{G,II}\tau_{GABA}}$ describes the competition of the pyramidal cells through the interneurons and $I_R(t)$ is determined by the scaled external stimuli and background noise.

2.2.6 The Partial Integro-Differential Equation for Multiple-Choice Decision Making. Combining the above simplifications, we obtain a partial integro-differential equation for the slow gating variable of NMDARs to explore the dynamics of multiple-choice decision making (see the bottom panel of Figure 1B). For simplicity, we have omitted the subscripts of NMDAR in the rest of this letter:

$$\frac{\partial S(\theta, t)}{\partial t} = -\frac{S(\theta, t)}{\tau_s} + \gamma[1 - S(\theta, t)]r(\theta, t), \tag{2.19}$$

$$r(\theta, t) = \frac{c_E I(\theta, t) - I_E}{1 - \exp[-g_E(c_E I(\theta, t) - I_E)]}, \tag{2.20}$$

$$I(\theta, t) = \int_0^{360} W(\theta' - \theta)S(\theta', t)\, d\theta' + I_{ext}(\theta, t) + I_{back} + I_{noise}(\theta, t), \tag{2.21}$$

where $W(\theta' - \theta) = J_{EE}\omega(\theta' - \theta) - J_{EIE}$, $I_{ext}(\theta, t)$ represents the equivalent task-related AMPAR-mediated synaptic current input to the θ-preferred excitatory pool. I_{Back} is the mean effective constant background input. J_{EE} is the effective NMDAR-mediated synaptic conductance. $I_{noise}(\theta, t)$ represents the equivalent noisy input. Here we choose these parameters as follows: $\tau_s = 100$ ms, $\gamma = 0.641$, $c_E = 320(VnC)^{-1}$, $I_E = 125$ Hz, $g_E = 0.16$ s, $J_{EE} = 0.0194$, $J_{EIE} = 0.0203$, and $I_{back} = 0.2702$ nA. Because the mean field approach does not take into account the time-varying noise that plays a crucial role in the spiking neuron model, we add a noise term implemented as white noise filtered by a short time constant (AMPA synaptic). This can be described as an Ornstein-Uhlenbeck process (Wong & Wang, 2006),

$$\tau_{AMPA}\frac{dI_{noise}(\theta, t)}{dt} = -I_{noise}(\theta, t) + \xi(\theta, t)\sqrt{\tau_{AMPA}\sigma^2_{noise}}, \tag{2.22}$$

where σ^2_{noise} is the variance of the noise ($\sigma_{noise} = 0.027$ nA), $\tau_{AMPA} = 2$ ms, and $\xi(\theta, t)$ is a gaussian white noise with zero mean and unit variance. In the simulations, we use a stable integration process for this gaussian stochastic model, which guarantees that the statistical properties of the variables are independent of the integration step (Destexhe, Rudolph, Fellous, & Sejnowski, 2001; Gillespie, 1996),

$$I_{noise}(\theta, t + h) = I_{noise}(\theta, t)e^{-\frac{h}{\tau_{AMPA}}} + AN(0, 1), \tag{2.23}$$

where $A = \frac{\sqrt{2}}{2}\sigma_{noise}\sqrt{1 - e^{-\frac{2h}{\tau_{AMPA}}}}$, and $N(0, 1)$ is a gaussian white noise with zero mean and unit variance. In the numerical simulation, we choose the integration step $h = 0.1$ ms.

2.3 The Task-Related External Stimuli. In the reduction model, the external input was constructed to model the multiple-choice task (Churchland et al., 2008). The external input to pyramidal cells consists of the following four parts: the visual stimulus about multiple alternatives, the random-dot motion stimulus, a top-down control signal, and the inhibitory input. The coherent motion is encoded by the neurons in the middle temporal area (MT), while the targets are encoded in a separate sensory area. These two types of signals relay to components of the decision circuit such as LIP. Meanwhile, the top-down control signal comes from higher brain areas such as the prefrontal cortex and can modulate the activities of LIP neurons during the task. The external inputs to the interneurons are transferred to inhibitory inputs to pyramidal cells through the linearization of the activation function of interneurons. In summary, we adopted the procedure of

Furman and Wang (2008) to model the external input to the pyramidal cells preferring θ as

$$I_{ext}(\theta,t) = J_{ext}\{I^{Tar}_{AMPA}(\theta,t) + I^{Mot}_{AMPA}(\theta,t)\} + I^{Control}_{AMPA}(\theta,t) - I^{Inh}_{AMPA}(\theta,t),$$

where the external input strength J_{ext} is equal to 1 unless otherwise noted. The target input, $I^{Tar}_{AMPA}(\theta,t)$, which reaches the LIP at 500 ms with a latency of 200 ms, depends on the number and location of the targets in the experiment (see Figure 1D) and varies with time,

$$I^{Tar}_{AMPA}(\theta,t) = h(t)\sum_{k=1}^{n_{tar}} \exp\left(-\frac{(\theta-\theta^k_{tar})^2}{\sigma^2_{tar}}\right), \tag{2.24}$$

where n_{tar} is the number of targets, θ^k_{tar} is the direction of the kth target, $\sigma_{tar} = 10^\circ$, and $h(t)$ is a time-dependent multiplier (see Figure 1C),

$$h(t) = \begin{cases} 0 & 0 < t < t_0 \\ a_1 + a_2\exp(-(t-t_0)/\tau_1) & t_0 \le t < t_1 + 80 \\ a_3 + (a_1 - a_3)\exp(-(t-t_1-80)/\tau_2) & t_1 + 80 \le t \end{cases} \tag{2.25}$$

where $t_0 = 500$ ms is the onset of targets and $t_1 = 1300$ ms is the onset of the motion stimuli. The time course of $h(t)$ is in accordance with the observations of the monkey experiment. The exponential decay of the target input's transient phase can be explained by the adaptation after the tonic stimulus. The suppression of the target input starting with a latency of 80 ms after the motion stimulus onset is assumed to be the result of either an attentional shift from the targets to the coherent motion of random dots or of cross-inhibition between upstream neurons encoding the targets and the motion stimulus (Furman & Wang, 2008); τ_2 describes the speed of decay. We chose $\tau_1 = 50$ ms, $\tau_2 = 15$ ms, $a_1 = 0.28$ nA, $a_2 = 0.15$ nA, and $a_3 = 0.06$ nA.

The motion stimulus from the MT to the LIP depends on the direction and coherence level of the motion. The profile of the motion stimuli can be approximated by a gaussian function, and its width is independent of the coherence level (see Figure 1E). However, the motion stimulus at zero coherence is a unified input to all selective pools. The motion signals reach LIP area at 1500 ms, with a latency of 200 ms (see Figure 1C). The motion stimulus is given by

$$I^{Mot}_{AMPA}(\theta) = b_0 + c'\left(-b_1 + b_2\exp\left(-\frac{(\theta-\theta_{mot})^2}{\sigma^2_{mot}}\right)\right), \tag{2.26}$$

where $c'(0 \le c' \le 1)$ denotes the coherence level and θ_{mot} is the random-dot motion direction. Here we used $b_0 = 0.002$ nA, $b_1 = 0.002$ nA, $b_2 = 0.01$ nA, and $\sigma_{mot} = 40^\circ$.

In our model, the top-down control signal is nonselective. We assumed the magnitude of the control signal to vary with the number of the choices and the phase during the target or motion stimulus. The control signal is given by

$$I_{control} = \begin{cases} 0 & 0 < t < t_0 \\ c_1 & t_0 \le t < t_1 + 200\,, \\ c_2 & t_1 + 200 \le t \end{cases} \tag{2.27}$$

where c_1 is 0.01 nA for two choices and 0.035 nA for four choices and c_2 is 0.0198 nA for two choices and 0.039 nA for four choices. The inhibitory input is also a nonselective signal during the target's presentation, does not vary with the number of choices, and contributes to stabilize the response of the system during the targets' presentation:

$$I_{inhibitory} = \begin{cases} 0 & 0 < t < t_0 \\ d_1 + d_2 \exp(-(t - t_0)/\tau_1) & t_0 \le t < t_1 + 80\,, \\ d_1 \exp(-(t - t_1 - 80)/\tau_2) & t_1 + 80 \le t \end{cases} \tag{2.28}$$

where $d_1 = 0.12$ nA, $d_2 = 0.03$ nA, and other parameters are identical to those in the target input.

2.4 Decision Readout. We assumed that the threshold for decision depends on neither the motion coherence level nor the number of choices according to the experimental observations. A decision is reached when any of the firing rates crosses a threshold of 60 Hz. The selected target is determined as that closest to the population vector (Furman & Wang, 2008):

$$\theta_p(t) = \arctan\left(\frac{\int_0^{360} r(\theta, t)\sin(\theta)\,d\theta}{\int_0^{360} r(\theta, t)\cos(\theta)\,d\theta}\right). \tag{2.29}$$

Meanwhile, the reaction time (RT) is calculated by,

$$RT = t_D - t_{start} + t_{post}, \tag{2.30}$$

where t_D is the time when the decision is made, $t_{start} = 1300$ ms is the onset of the motion stimulus, and $t_{post} = 80$ ms is the postreaction time due to the execution of the saccade.

3 The Numerical Integration of Partial Integro-Differential System

The partial integro-differential system, equations 2.19 to 2.21, describes the dynamics of multiple-choice decision making. In this section, we demonstrate that the typical behaviors of multiple-choice decision making can be captured by the reduced system using numerical integration.

3.1 Time Course of the Multiple-Choice Decision Making. In our model, the continuous selective pools are thought to represent the populations of pyramidal cells in LIP. Several sample simulation trials for two- and four-choice decision making with 0% coherence, called unbiased decision making, are shown in Figure 2. Before the onset of the target input, all selective pools in this local microcircuit display spontaneous activity. Once the target stimuli are presented, the system develops a series of strong, localized activity bumps centered in the direction of the targets, a behavior similar to those in the spiking network (Furman & Wang, 2008). These activity bumps are identical in height and shape. Because both the target stimuli and the nonselective inhibitory input are very strong during the target presentation, these activity bumps are stable, and the network does not exhibit the winner-take-all mechanism. When the motion stimulus is presented, the populations located around the targets undergo a dip in activity due to a decrease in the target caused by either divided attention or the upstream inhibition of the target signal. As the activities develop in response to the motion stimulus, the stochastic recurrent inputs gradually break the symmetry between the activity bumps, even though the mean total external inputs to the network are symmetric over time. The activity of the pyramidal pool located around the selected target ramps up and wins the competition, while the activities of the other neuron pools ramp down and lose the competition. The decision process ends when the activity of the ramping-up pool reaches the predetermined threshold. For simplification, we set the threshold as 60 Hz, where it was dependent on neither the coherence level nor the number of choices.

We have simulated two- and four-choice decision making with a nonzero coherence level (i.e., the biased decision making). In biased decision making, the target inputs to the network are still symmetric among the target directions. Once the biased stimuli are presented, the total inputs to the network are asymmetric, and the network starts to accumulate differences between the motion direction and other directions until one target wins the competition. The spatiotemporal pattern of the neural activity is similar to the pattern of unbiased decision making. The average firing rate of the neuron pools located around the selected target ramps up, while the average firing rates of the neuron pools located at other targets ramp down for two- and four-choice decision making in correct trials. The increased coherence level leads to a steeper ramping up and a shorter reaction time (see Figure 3). The numerical integration resulting from the partial integro-differential

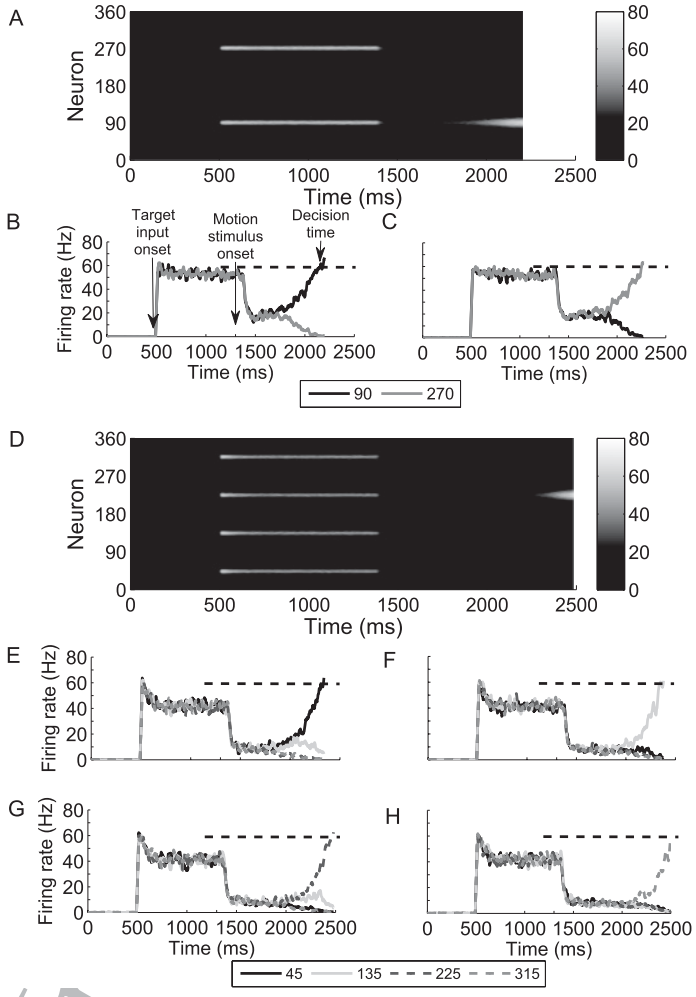

Figure 2: Neural activities for two- and four-choice decision making. (A, D) Spatiotemporal activity of the pyramidal neuron pool in the reduction model. Pyramidal neurons are arranged along the ordinate according to their preferred directions. The directions of the targets for two alternatives are 90° and 270°, while the directions of the targets for four choices are 45°, 135°, 225°, and 315°. When the number of the choices increases, the target inputs and the top-down control signal are modified accordingly, but the motion stimulus and all model parameters are fixed. The reduced model is capable of making a decision in the visual motion discrimination task independent of the number of the alternatives. (B–C, E–F) Activity time course of neural pools located around the targets when the number of choices is two and four, respectively.

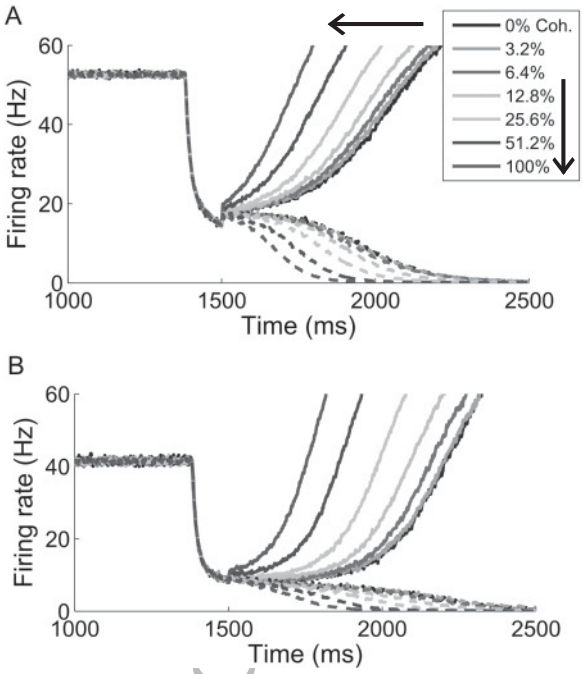

Figure 3: The firing rate time course of the neuron pool located around the selected target (solid lines) and the opposite direction (dashed lines) are shown for (A) two-choice and (B) four-choice decision making. The average firing rate was obtained by averaging the neural activity over 200 correct trials. The line with different gray scale denotes the different coherence levels shown as in the legend.

equation (see Figures 2 and 3) is consistent with that of the spiking network model (Furman & Wang, 2008) and agrees with the experimental observations (Churchland et al., 2008).

3.2 Accuracy and Reaction Time. The behaviors of the partial integro-differential equation are consistent with the experimental observations (see Figure 4). The accuracy (percentage of correct choices) deteriorates with increasingly difficult tasks. On the one hand, a higher coherence level favors higher accuracy. When the coherence level is zero, the network behaves randomly and chooses each target with an equal probability. The network always makes the correct decision when the coherence level is greater than 50%. On the other hand, the accuracy varies with the number of targets. The accuracy of two-choice decision making is higher than that of four-choice decision making, given the same coherence level. These results are

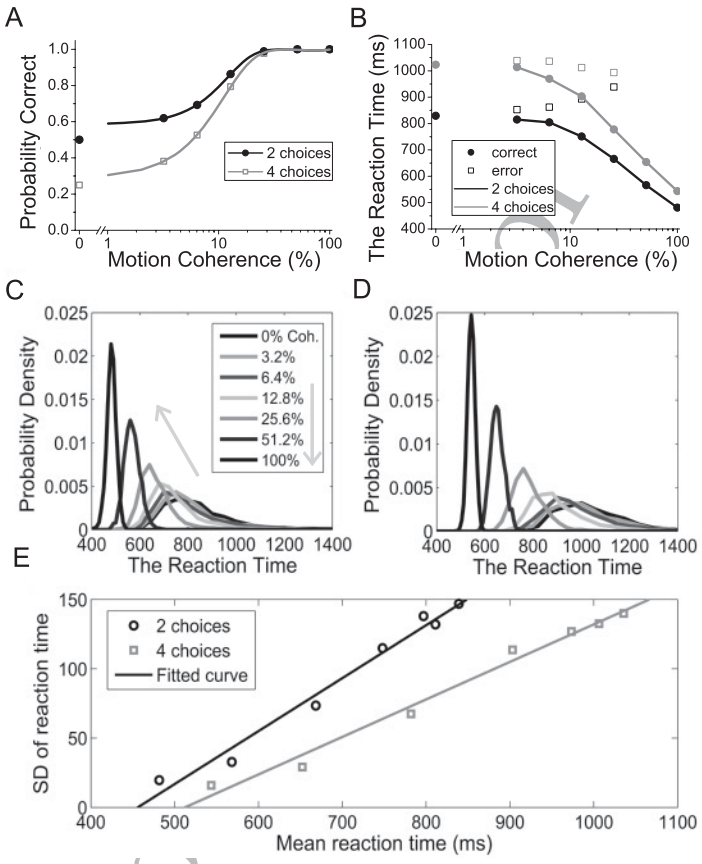

Figure 4: Performance and reaction time of the model. (A) Correct rate of choice, given different coherence levels for two- and four-choice decision making. A higher coherence level leads to a higher rate of correct choice, and the correct rate of two-choice decision making is higher than that of four-choice decision making. The line is Weibull fitting to the data. (B) The mean reaction time decreases as the coherence level increases and the number of choices decreases. Incorrect decisions take longer than correct ones. The filled circles represent correct trials, and open squares represent erroneous trials. (C, D) Distribution of the reaction time for correct two- and four-alternative decision making, respectively. The reaction time follows an asymmetric distribution. (E) The standard deviation of the reaction time is linearly related to the mean reaction time, implying that the reaction time obeys Weber's law.

in agreement with the monkey experiments (Romo & Salinas, 2001; Shadlen & Gold, 2004; Churchland et al., 2008) and the simulations of the spiking network model (Wang, 2002; Furman & Wang, 2008).

The reaction time is another important quantity to measure the decision process. Because of the noisy background input, the reaction time varies from trial to trial. We calculated the mean and distribution of the reaction time given different coherence levels and different target numbers (see Figures 4B–4E). For correct trials, the mean reaction time decreases as the coherence level increases. The time required for decision making increases in the presence of a low coherence level and a large number of tasks, in the sense that it takes longer for the network to accumulate evidence for difficult tasks. The mean reaction time for an incorrect trial is much longer than that for a correct trial. The distribution of reaction time, shown in Figures 4C and 4D for two- and four-choice decision making, respectively, has several features. First, higher coherence levels result in distributions with smaller means and variances. Lower coherence levels lead to distributions with larger means and variances. Second, the distribution of the reaction time is asymmetric. The probability sharply ramps up to the peak at the left and slowly ramps down to the right. Third, the standard deviation is positively and linearly related to the mean. We plotted the mean and standard deviation of the reaction time in Figure 4E, which demonstrates that these values follow a linear relationship, with $SD = a + bRT$, where $a = -174$ and $b = 0.382$ for two-choice decision making, and $a = -138$ and $b = 0.2707$ for four-choice decision making. This result indicates that the reaction time obeys the psychophysical Weber's law (Deco & Rolls, 2006; Deco, Scarano, & Soto-Faraco, 2007).

4 The Nonlinear Dynamics Approach to the Decision Process

The numerical simulation results demonstrate that the partial integro-differential system, equations 2.19 to 2.21, accurately represents the multiple-choice decision making. In this section, we apply the nonlinear dynamics approach to reveal the dynamical mechanism giving rise to multiple-choice decision making. Considering the periodic boundary condition and the symmetric connectivity, the system 2.19 to 2.21 can be transformed into a series of ordinary equations by simple discretization in the space dimension, as follows:

$$\frac{dS_i(t)}{dt} = -\frac{S_i(t)}{\tau_s} + \gamma(1 - S_i(t))\phi_i(t), \quad i = 1, 2 \ldots N, \tag{4.1}$$

$$I_i(t) = \sum_{j=1}^{N} W((j-i)\Delta\theta)S_j\Delta\theta + I_{ext,i} + I_{back}, \tag{4.2}$$

where $\Delta\theta = \frac{360}{N}$, that is, the direction interval after the equidistant discretization, and $N = 1024$. By omitting the noisy term $I_{noise}(\theta, t)$ whose mean is zero and setting the right-hand side of the ordinary equations as

zero, we can calculate the steady states, $\bar{S}$, of the system without noise using Newton's method (Press, Teukolsky, Vetterling, & Flannery, 1992). The stability of the steady state is explored by introducing the perturbation $\delta\vec{S}(t)$ to the steady state, and the system state becomes $\vec{S}(t) = \vec{\bar{S}} + \delta\vec{S}(t)$. We considered the evolution of the perturbation that follows the dynamics,

$$\frac{d\delta\vec{S}(t)}{dt} = A\delta\vec{S}(t), \tag{4.3}$$

where A is a matrix and its component is

$$A(i,\, j) = \begin{cases} -\left(\dfrac{1}{\tau_s} + \gamma\phi_i\right) + \gamma\Delta\theta[1 - \vec{\bar{S}}_i]\phi_i' W((j-i)\Delta\theta), & i = j \\ \gamma\Delta\theta[1 - \vec{\bar{S}}_i]\phi_i' W((j-i)\Delta\theta), & i \neq j \end{cases}.$$

This matrix is steady state dependent, and its eigenvalues, λ_i, determine the stability of the steady state. If the eigenvalue λ_i is positive (negative), the steady state is unstable (stable) and the system will evolve away from (approach) the steady state along the corresponding eigenvector $\vec{v}_i$ (Strogatz, 2001).

4.1 Unbiased Decision Making

4.1.1 Stable Steady States for Two- and Four-Choice Unbiased Decision Making After the Motion Stimulus Reaches the LIP. The steady states of the system 2.19 to 2.21 play important roles in the decision process. For two-choice decision making, there are two stable steady states (see Figure 5A). Each stable steady state has a high bump centered at the direction of one target and a very small bump centered at the other direction. For four-choice decision making, there are four stable steady states (see Figure 5B). Each stable state has one high bump and three small bumps. The high bump localizes at the direction of one target, and the small bumps are located at the directions of the other targets. These stable steady states are absorbing attractors of the system. No matter where the initial state is located, the network will eventually approach one of these stable states and finally choose the target at which the high bump of the stable steady state localizes. Notably, the number of stable states is determined by the number of the targets.

4.1.2 Unstable Steady States for Two- and Four-Choice Unbiased Decision Making After the Motion Stimulus Reaches the LIP. Unstable steady states are more complex than stable steady states. For two-choice decision making, there are three types of unstable steady states (see Figure 5C). The first one, $\vec{\bar{S}}_{u,1}$, has two identical bumps, each corresponding to one target (see

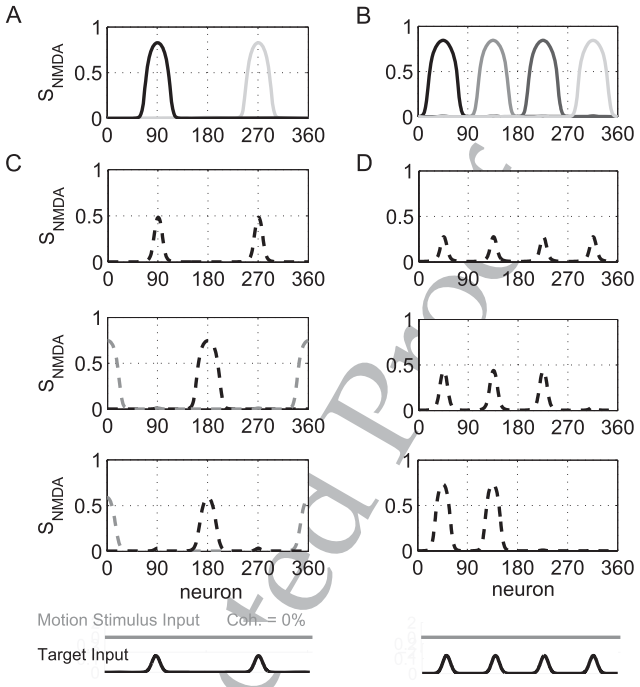

Figure 5: Steady states of the reduced system. (A, B) Stable steady states. (A) There are two one-bump stable steady states for two-choice decision making and (B) four one-bump stable steady states for four-choice decision making. The directions of the targets for two alternatives are 90° and 270°, while the directions of the targets for four choices are 45°, 135°, 225°, and 315°. The motion stimuli and target inputs are shown at the bottom. (C, D) Unstable steady states. (C) There are five unstable steady states for two-choice decision making, which are denoted as $\vec{\vec{S}}_{u,1}$, $\vec{\vec{S}}_{u,2}$, $\vec{\vec{S}}_{u,3}$, $\vec{\vec{S}}_{u,4}$, and $\vec{\vec{S}}_{u,5}$ from top to bottom, respectively. $\vec{\vec{S}}_{u,1}$ has two bumps with the same height, and these are located at the targets. $\vec{\vec{S}}_{u,2}$ and $\vec{\vec{S}}_{u,3}$ have one high bump, which is centered between the targets. $\vec{\vec{S}}_{u,4}$ and $\vec{\vec{S}}_{u,5}$ have one large bump, which is located between the targets and two small bumps centered at the targets. $\vec{\vec{S}}_{u,1}$ is responsible for decision making. (D) The three types of unstable steady states for four-choice decision making are relevant to the dynamics of the decision process and are denoted as $\vec{\vec{S}}_{u,1}$, $\vec{\vec{S}}_{u,2}$, and $\vec{\vec{S}}_{u,3}$ from top to bottom, respectively. The number of each type of unstable steady states is equal to the number of the combination: four combination, three combination, and two combination from four targets, respectively.

the upper panel of Figure 5C). The second type of unstable steady state, which includes $\vec{\vec{S}}_{u,2}$ and $\vec{\vec{S}}_{u,3}$, has one bump located between two targets (see the second panel of Figure 5C). The third type of unstable steady state,

which includes $\vec{\bar{S}}_{u,4}$ and $\vec{\bar{S}}_{u,5}$, has one intermediate high bump, with two small bumps located at the targets (see the bottom panel of Figure 5C). For four-choice decision making, there are five types of unstable steady state (see Figure 5D). The first type, $\vec{\bar{S}}_{u,1}$, has only one unstable steady state with four identical bumps located at each target. The second type of unstable steady state, $\vec{\bar{S}}_{u,2}$, has three high bumps and one low bump. Each bump of this type of unstable steady state is centered on the target. Because the low bump can be centered on any one of the targets, this type has four different steady states. The third type of unstable state, $\vec{\bar{S}}_{u,3}$, has two high bumps and two low bumps. Each bump centers at the targets, and there are six different unstable steady states. The fourth type of unstable steady state, $\vec{\bar{S}}_{u,4}$, has one high bump, which localizes between two targets. Thus, there are four unstable steady states belonging to this type. The last type of unstable steady states, $\vec{\bar{S}}_{u,5}$, has one high bump located between two targets and four small bumps located at the targets. For clarity, Figure 5D displays only one unstable steady state for each of first three types. In addition to the four identical bumps steady state $\vec{\bar{S}}_{u,1}$, the number of other types of unstable steady states is equal to the combination of high bumps and small bumps. Therefore, there are 1, 4, 6, 4, and 4 for each type of unstable steady state.

4.1.3 Dynamics in the Vicinity of the Unstable Steady States and the Decision Process Without Noise. Given a steady state $\vec{\bar{S}}$, the evolution of the system in the vicinity of the steady state can be approximated as (Strogatz, 2001)

$$\vec{S}(t) = \vec{\bar{S}} + \sum_{i=1}^{N} c_i e^{\lambda_i t} \vec{v}_i, \tag{4.4}$$

where N is the number for the space dimension discretization, λ_i is the ith eigenvalue, $\vec{v}_i$ is the corresponding eigenvector, and the coefficient c_i is the projection coefficient of the difference between the initial state $\vec{S}_0$ and the steady state $\vec{\bar{S}}$ on the ith eigenvector $\vec{v}_i$:

$$c_i = \frac{\vec{v}_i^T(\vec{S}_0 - \vec{\bar{S}})}{\vec{v}_i^T \vec{v}_i}. \tag{4.5}$$

Equation 4.4 indicates that the system contracts on the invariant manifold, which is tangent to the eigenvector with a negative eigenvalue, and expands in the invariant manifold tangent to the eigenvector with a positive eigenvalue. As the result of the expansion in the invariant manifold tangent to the eigenvector with the positive eigenvalue, the system will evolve away from the unstable steady states and eventually approach one of the stable steady states, finally leading to a decision among the targets. As mentioned

above, the activity bumps are stable during the targets' presentation because the inhibitory input is strong during that time. This phenomenon has been demonstrated by the fact that the two-bump state for two choices and the four-bump state for four choices are always stable when analyzed similar to the method in Figure 9A. After the motion stimulus onset, both the target and inhibitory inputs will gradually decrease, and these states will become unstable. The system is gradually driven toward the vicinity of the unstable steady state $\vec{\bar{S}}_{u,1}$ for both two and four choices. Therefore, we focused on the dynamics of the system in the vicinity of the unstable steady states, especially $\vec{\bar{S}}_{u,1}$.

For two-choice decision making, we calculated the spectrum of the unstable steady state $\vec{\bar{S}}_{u,1}$, which has two equal bumps. We found that only one eigenvalue λ_0 is positive (see Figure 6A), while the others are negative. We also calculated the corresponding eigenvectors and found that the upward and downward bumps in the eigenvector corresponding to that positive eigenvalue (see Figure 6A) demonstrate the competition between two targets. Given any initial state in the vicinity of the steady state $\vec{\bar{S}}_{u,1}$, the projection coefficient c_i can be calculated according to formula 4.5. The coefficient c_0 determines the choice of decision making because the system shrinks to the steady state in the manifold tangent to the eigenvector with a negative eigenvalue and expands in the manifold tangent to the eigenvector with a positive eigenvalue. If $c_0 > 0$, the activity of the 270°-selective pool increases, and the activity of the 90°-selective pool decreases, which causes the 90° target to lose the competition. If $c_0 < 0$, the firing rate of the 270° preferring neurons decreases while the firing rate of the 90° preferring neurons increases, causing the 270° target to lose the competition.

For clarity, we showed the time evolution of the system in Figure 7. Starting from an initial state, which is set as the subtraction of the steady state by a small perturbation $\vec{S} = \vec{\bar{S}} - \Delta\vec{S}$, we can numerically approximate the time evolution of the system according to formula 4.4. In Figure 7A, we chose a special perturbation $\Delta\vec{S}$ with $c_0 = -0.1$ and $c_i = 0 (i \neq 0)$. The figure shows that the firing rate of the 90°-selective pool increases and the firing rate of the 270°-selective pool decreases over time. We also show three other examples in Figure 7B. The perturbation of the first two are deterministic with the parameters $c_0 < 0$, $c_i = 0 (i \neq 0)$, and $c_0 > 0$, $c_i = 0 (i \neq 0)$, and the third perturbation is random with $c_0 = -0.0123$. The results confirm that c_0 determines which target will win the competition.

For four-choice decision making, we also calculated the spectrum of each unstable steady state. Similar to the case of two choices, the local dynamics in the vicinity of $\vec{\bar{S}}_{u,1}$ also plays a major role in the early stage of four-choice decision making. The steady state $\vec{\bar{S}}_{u,1}$ has only one positive triplet eigenvalue (see Figure 6B), and the other eigenvalues are negative. The corresponding eigenvectors of the positive triplet eigenvalues are $\vec{v}_{0,0}$, $\vec{v}_{0,1}$, and $\vec{v}_{0,2}$ (see Figure 6B). $\vec{v}_{0,0}$ has two upward bumps at 135° and 315° and

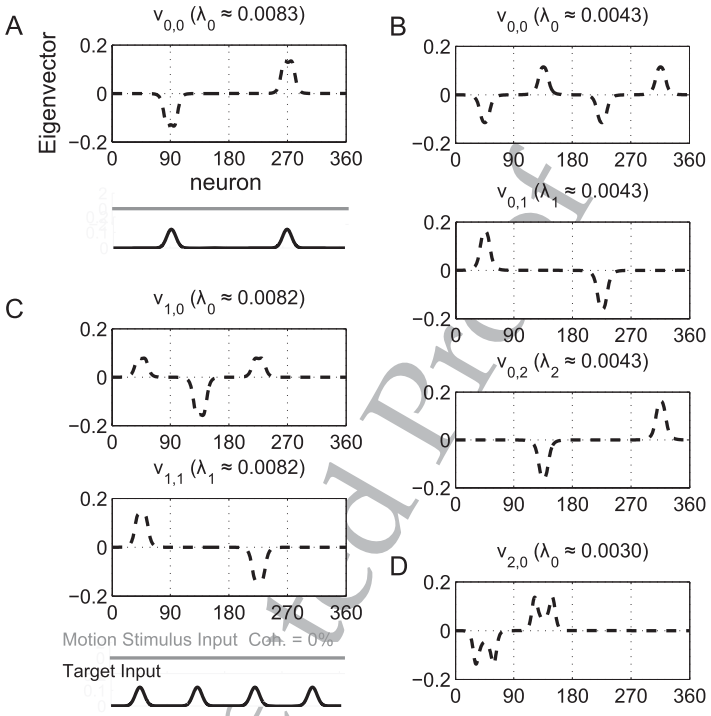

Figure 6: Examples of the eigenvectors of the unstable steady states, where the dashed line denotes an eigenvector with a positive eigenvalue. (A) The eigenvector of the unstable steady state $\vec{\vec{S}}_{u,1}$ for two-choice decision making with a positive eigenvalue. (B) The unstable steady state $\vec{\vec{S}}_{u,1}$ for four-choice decision making has three identical positive eigenvalues, and the corresponding eigenvectors are shown from top to bottom. (C) The unstable steady state $\vec{\vec{S}}_{u,2}$ for four-choice decision making has two identical positive eigenvalues and the corresponding eigenvectors shown from top to bottom. (D) The unstable steady state $\vec{\vec{S}}_{u,3}$ for four-choice decision making has only one positive eigenvalue. The eigenvector for this positive eigenvalue is similar to the eigenvector in panel A.

two downward bumps at 45° and 225°. $\vec{v}_{0,1}$ has one upward bump at 45° and one downward bump at 225°, and $\vec{v}_{0,2}$ has one upward bump at 315° and one downward bump at 135°. From the eigenvector $\vec{v}_{0,0}$, we can view two upward bumps as the vertical group and two downward bumps as the horizontal group, and this eigenvector depicts the competition between these two groups in the early stage of decision making. In addition, the eigenvectors $\vec{v}_{0,1}$ and $\vec{v}_{0,2}$ depict the competition between two bumps in each group. Given an initial state close to $\vec{\vec{S}}_{u,1}$, the coefficients c_0, c_1, and

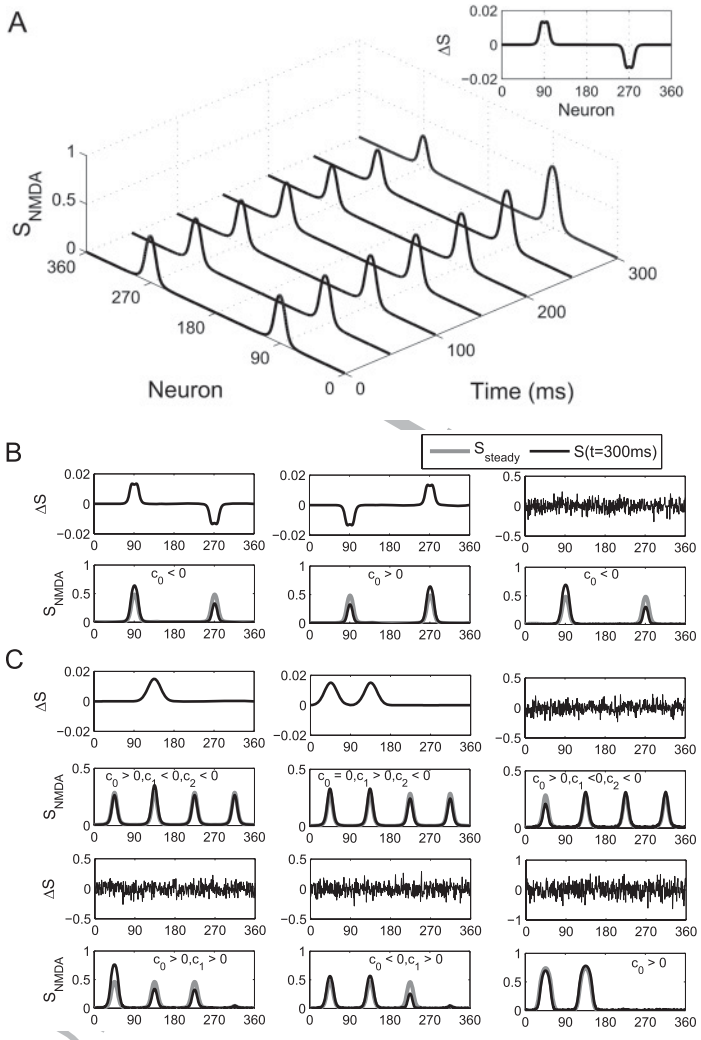

Figure 7: The evolution of noise-free decision making. (A) The evolution of noise-free two-choice decision making, given the perturbation of ΔS as shown in the (inset), where $c_0 = -0.1$ and $c_i = 0$ for $i > 0$. (B) The unstable steady state $\vec{S}_{u,1}$ for two-choice decision making and the state at 300 ms given different ΔS perturbations, as shown in the top row. (C) The perturbation and the state at time 300 ms. Three different perturbations to $\vec{S}_{u,1}$ for four-choice decision making are shown in the first row, and the corresponding time evolution is shown in the second row. Two different perturbations to $\vec{S}_{u,2}$ and one perturbation to $\vec{S}_{u,3}$ for four-choice decision making are shown in the third row, and the corresponding time evolutions are shown in the bottom row.

Table 1: The Winning Target Given Unitary Perturbation to $\vec{S}_{u,1}$.

c_0	$+1$	$+1$	$+1$	$+1$	-1	-1	-1	-1
c_1	$+1$	$+1$	-1	-1	$+1$	$+1$	-1	-1
c_2	$+1$	-1	$+1$	-1	$+1$	-1	$+1$	-1
Winner	315°	135°	315°	135°	45°	45°	225°	225°

c_2 determine how the system evolves away from the unstable steady state. For example, if $c_0 = +1$, $c_1 = +1$ and $c_2 = +1$, the increase of activity at approximately 45° caused by $v_{0,1}^{\rightarrow}$ will almost be canceled by the decrease of activity caused by $v_{0,0}^{\rightarrow}$, and the same is true for the activity at approximately 135°. However, the activity at approximately 225° will decrease, and the activity of approximately 315° will increase. The different combination of the coefficients could lead different targets to win the early competition between targets (see Table 1). Usually, the increase of activity to one target caused by one eigenvector could not be canceled by the decrease of activity to the same target caused by other eigenvectors because the coefficients are not equal to ± 1 and the system will be driven toward the unstable steady state with three or two bumps: $\vec{S}_{u,2}$ or $\vec{S}_{u,3}$. $\vec{S}_{u,2}$ has three equal-height bumps located at 45°, 135°, and 225° and one very small bump located at 315° with one positive doublet of eigenvalues (see Figure 6C). The positive doublet eigenvalues correspond to two eigenvectors (see Figure 6C), $\vec{v}_{1,0}$ and $\vec{v}_{1,1}$. $\vec{v}_{1,0}$ has two upward bumps located at 45° and 225° and one downward bump located at 135°. $\vec{v}_{1,1}$ has one upward bump located at 45° and one downward bump located at 225°. $\vec{S}_{u,2}$, which has two identical bumps located at 45°and 135°, has only one positive eigenvalue (see Figure 6D). The eigenvector corresponding to this positive eigenvalue $\vec{v}_{2,0}$ has one upward bump and one downward bump (see Figure 6D), a fact that supports the competition between two bumps. As examples of the evolution of the system in the vicinity of unstable steady state, we perturbed $\vec{S}_{u,1}$, $\vec{S}_{u,2}$, and $\vec{S}_{u,3}$ using different $\Delta\vec{S}$. The competition between targets can be displayed by the coefficients of the projection of $\vec{S}_0 - \vec{S}$ on the eigenvectors (see Figure 7C).

4.2 Biased Decision Making. For unbiased decision making, the basic mechanism underlying decision making is that the system will evolve away from the unstable steady state with equal bumps, and the unstable invariant manifold starts from the unstable steady state, which breaks the symmetry of the inputs. For biased decision making, the system is driven to a state with equal bumps by the target signal before the motion signal reaches the decision area. The initial state is close to the unstable steady state after the signal of asymmetric motion arrives at the decision area. The unstable steady states of the system change due to the inputs of asymmetric motion.

The reaction time and the performance of decision making also change with the asymmetric motion input.

4.2.1 Steady States of Biased Two-Choice Decision Making After the Motion Signal Reaches the LIP. Given an asymmetric input or nonzero coherence level, the system 2.19 to 2.21 for two-choice decision making has two stable steady states and five unstable steady states (see Figure 8A). The stable steady states are located in the direction of the targets and are responsible for the choice. The unstable steady states have significant differences from those of unbiased decision making. First, the symmetry of the two-bump unstable state $\vec{\vec{S}}_{u,1}$ is broken. The height of the bump centered in the coherent motion direction is lower than that of the other bump. The difference between two bumps is almost linearly correlated with the motion coherence, and a higher coherence level leads to a larger difference (see Figure 8D). Second, the higher bump of the unstable steady states, $\vec{\vec{S}}_{u,2}$ and $\vec{\vec{S}}_{u,3}$, whose higher bumps localize between the targets, shifts toward the direction opposite to the coherent motion. This shift intuitively seems to enlarge the attractive basin for the stable steady state corresponding to the correct choice.

Before the onset of the motion stimulus, the target inputs are symmetrical, and the system is driven to the initial state, which has two identical bumps and is close to the unstable steady state $\vec{\vec{S}}_{u,1}$. Therefore, we analyzed the local dynamics of this unstable steady state. Similar to the unbiased scenarios, $\vec{\vec{S}}_{u,1}$ has only one positive eigenvalue, and the corresponding eigenvector, $\vec{v_0}$, has one upward bump and one downward bump located at the targets. This eigenvector underlies the competition between two targets (see the first panel of Figure 8C).

4.2.2 Steady States of Biased Four-Choice Decision Making After the Motion Signal Reaches the LIP. The steady states of the system 2.19 to 2.21 for four-choice decision making with biased motion stimulus are similar to those for unbiased four-choice decision making. The system has four stable steady states. Each of these has one high bump located in the direction of the target and is responsible for the final choice. The system still has five types of unstable steady states, which are similar to unstable steady states of the system responsible for unbiased four-choice decision making. For simplicity, we have shown only an example for $\vec{\vec{S}}_{u,1}$, $\vec{\vec{S}}_{u,2}$, and $\vec{\vec{S}}_{u,3}$ in Figure 8B. The unstable steady states are influenced by asymmetric motion stimuli. First, the symmetry between the four bumps of the unstable steady state $\vec{\vec{S}}_{u,1}$ is broken. The bump located in the direction of the motion shrinks and becomes lower than the other three bumps, which are identical in height. A higher coherence level leads to a larger difference between the bumps (see Figure 8E). Second, the eigenvalues of the four-bump unstable steady state $\vec{\vec{S}}_{u,1}$ change significantly (see the last three panels of Figure 8C). The positive triplet eigenvalues become one positive singlet and one positive doublet of

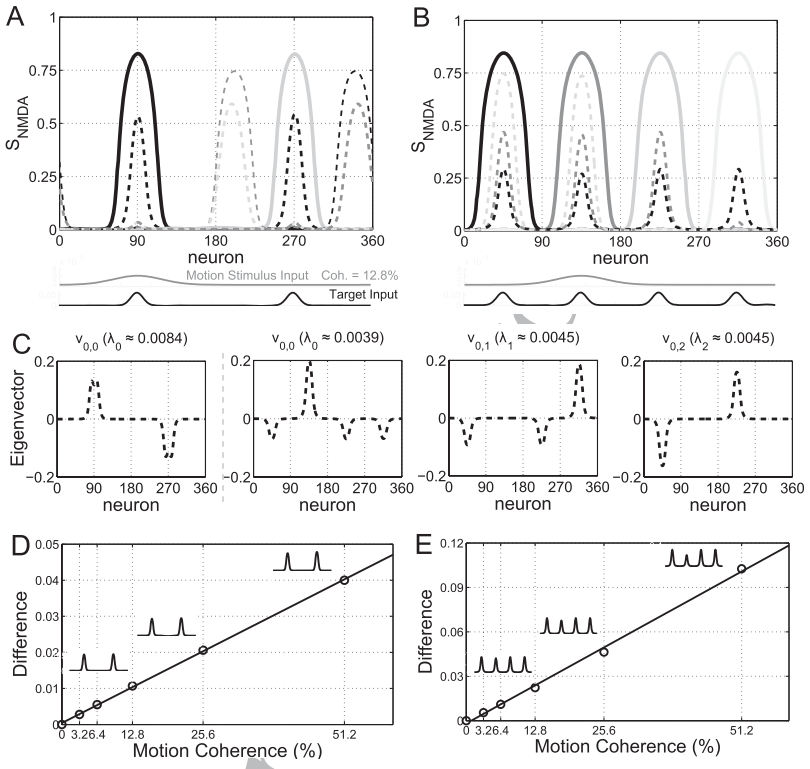

Figure 8: Biased decision making. (A) The steady states of the system after the motion stimuli and target signals arrive at the decision area for two-choice decision making. The system has two stable steady states denoted by solid lines and five unstable steady states denoted by dashed lines. The unstable steady states $\vec{\vec{S}}_{u,2}$ and $\vec{\vec{S}}_{u,3}$ shift in the direction opposite the motion stimuli. (B) The steady states of the system after the motion signal stimuli arrive at the decision area for four-choice decision making. The system has four stable steady states denoted by solid lines, and the numbers of the unstable steady states are denoted by dashed lines (not all of the unstable steady states are shown here). (C) For two alternatives, there is only one positive eigenvalue for the unstable steady state $\vec{\vec{S}}_{u,1}$. The eigenvector corresponding to the positive eigenvalue $\vec{v}_0$ is shown in the first panel. For four choices, there are three positive eigenvalues for the unstable steady state $\vec{\vec{S}}_{u,1}$, and the corresponding eigenvectors are shown in the remaining panels. (D, E) The difference between the height of the two or four bumps of the unstable steady state $\vec{\vec{S}}_{u,1}$ linearly increases with increasing coherence levels.

Table 2: The Winner Given the Unitary Perturbation of $\vec{\vec{S}}_{u,1}$ as Shown in the Last Three Panels of Figure 8.

c_0	$+1$	$+1$	$+1$	$+1$	-1	-1	-1	-1
c_1	$+1$	$+1$	-1	-1	$+1$	$+1$	-1	-1
c_2	$+1$	-1	$+1$	-1	$+1$	-1	$+1$	-1
Winner	135°	135°	135°	135°	315°	315°	225°	45°

eigenvalues. Third, the eigenvectors corresponding to positive eigenvalues of the unstable steady state $\vec{\vec{S}}_{u,1}$ also undergo remarkable changes. The eigenvector $\vec{v}_{0,0}$, has three small downward bumps and one large upward bump. The upward bump is located in the direction of the motion, and this eigenvector favors the correct choice. Fourth, the unstable steady states $\vec{\vec{S}}_{u,4}$ and $\vec{\vec{S}}_{u,5}$, whose bumps are located between two targets, shift away from the motion direction (not shown).

4.2.3 Dynamics in the Vicinity of the Unstable Steady State $\vec{\vec{S}}_{u,1}$ and the Decision Process Without Noise. Although the motion stimulus is biased, the initial state of the system, $\vec{S}_0$, has identical bumps located at each of the targets because the target signal and the top-down control signal are symmetric. Therefore, the system is set in the vicinity of the unstable steady state $\vec{\vec{S}}_{u,1}$ and the early stage of the decision process is determined by the local dynamics of the steady state as described by formula 4.4.

For biased two-choice decision making, the coefficient of c_0 also determines the final choice. Given a positive c_0, the 90° target will win the competition, while the 270° target will win the competition given a negative c_0. Due to the symmetric initial state $\vec{S}_0$, and the asymmetric unstable steady state $\vec{\vec{S}}_{u,1}$, the difference of $\vec{S}_0 - \vec{\vec{S}}_{u,1}$ has one small upward bump, which is located in the direction of the motion because the bump of $\vec{\vec{S}}_{u,1}$, located in the motion direction, is lower than the other bump. If the motion direction is 90°, $\Delta\vec{S}$ should have a small upward bump located at 90° in the same direction as the eigenvector $v_{0,0}$ (see Figures 8A and 8C). Thus, the coefficient $c_0 > 0$ and the activity of neurons preferring 90° will increase and lead to the choice of the 90° target. If the motion direction is 270°, the lower upward bump of the unstable steady state $\vec{\vec{S}}_{u,1}$ will be located at 270°. The eigenvalue, eigenvector, and the coefficient c_0 will change accordingly. The dynamic process is similar, and the system will choose the target at 270°.

For biased four-choice decision making, the combination of the first three projection coefficients determines the final choice (see Table 2). For example, given the combination of $c_0 = -1, c_1 = -1$, and $c_2 = +1$, the activity approximately at 135° and 315° will decrease due to the larger bump located at 315° in the second eigenvector $\vec{v}_{0,1}$. Finally, the activity at approximately

225° will increase following the third eigenvector $\vec{v}_{0,2}$. Similar to biased two-choice decision making, the difference of $\Delta\vec{S} = \vec{S}_0 - \vec{\bar{S}}_{u,1}$ has one small upward bump, which is located in the motion direction because the bump of $\vec{\bar{S}}_{u,1}$, located in motion direction, is lower than the other three bumps. In the example shown in Figure 8B, the motion direction is 135°, and the bump of $\vec{\bar{S}}_{u,1}$, located at 135°, is lower, and $\Delta\vec{S}$ has one small upward bump located at 135°. Thus, the dominant term of the projection of $\Delta\vec{S}$ onto the eigenvectors should be the projection onto the eigenvector $\vec{v}_{0,0}$ with a positive coefficient c_0. This implies that the eigenvector $\vec{v}_{0,0}$ dominates the evolving-away process, the activity of neurons preferring 135° will increase, and the system will choose the target at 135°.

As a summary of the nonlinear analysis, we explored the dynamical architecture of the partial integro-differential system underlying two- and four-alternative decision making. There are several notable differences between two- and four-choice decision making. First, the number of stable steady states representing the decision options is different and equals the number of targets. Second, the decision process for four choices is not only related to the unstable manifolds of the unstable steady state with the four identical bumps of $\vec{\bar{S}}_{u,1}$, but also to those of other unstable steady states, such as $\vec{\bar{S}}_{u,2}$ and $\vec{\bar{S}}_{u,3}$. Three unstable manifolds of the steady state $\vec{\bar{S}}_{u,1}$ make the system evolve toward any of stable and unstable states except $\vec{\bar{S}}_{u,1}$. Two unstable manifolds of the steady state $\vec{\bar{S}}_{u,2}$ lead to the system's evolution toward any of the steady states except $\vec{\bar{S}}_{u,1}$ and $\vec{\bar{S}}_{u,2}$. One unstable manifold of the steady states $\vec{\bar{S}}_{u,3}$ guides the system to evolve toward any of stable states. The structure composed of these three types of unstable steady states predominates the system's evolution from the initial state to one of the stable states for a decision process with four choices.

4.3 Parameter Ranges of the Network Supporting Decision Making. In numeric simulations and nonlinear analysis, only the top-down control signal and the number of neuron pools receiving the target inputs vary with the number of choices. The other parameters remain unchanged, indicating that the parameters of the network support either two- or four-choice decision making. Therefore, it is important to know the dependence of the results on the parameters we used. Considering that the system can make a decision if its steady state, $\vec{\bar{S}}_{u,1}$, is unstable for two-choice decision making and that the steady states $\vec{\bar{S}}_{u,1}$, $\vec{\bar{S}}_{u,2}$, and $\vec{\bar{S}}_{u,3}$ are unstable for four-choice decision making, we could calculate the steady states and show their stability by variation of parameters, including the external input strength J_{ext} and the iso-directional connection strength J^+.

For simplification, we considered only unbiased decision making. In Figure 9A, we showed the influence of J_{ext} on the peak value and the stability of the steady states $\vec{\bar{S}}_{u,1}$, $\vec{\bar{S}}_{u,2}$, and $\vec{\bar{S}}_{u,3}$ for unbiased four-choice decision

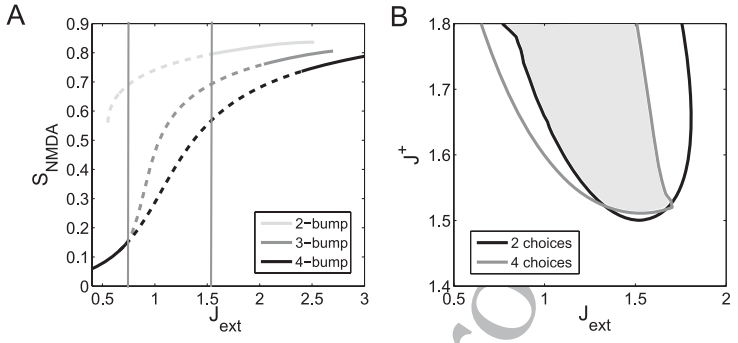

Figure 9: Parameter ranges of the network supporting decision making. (A) The peak of the highest bump of the unstable steady states $\vec{\vec{S}}_{u,1}$, $\vec{\vec{S}}_{u,2}$, and $\vec{\vec{S}}_{u,3}$ as a function of the external input strength J_{ext} for four choices. Solid (dashed) lines indicate that the corresponding states are stable (unstable). The parameter in the interval between two vertical lines supports a decision. (B) The overlapping parameter domains for two- and four-choice decision making. The parameter ranges supporting decisions are enveloped by the dark curve for two choices and the gray curve for four choices.

making. The peaks of these steady states increase with increasing J_{ext}. The four-bump steady state $\vec{\vec{S}}_{u,1}$ is stable when J_{ext} is small and becomes unstable as J_{ext} increases, finally becoming stable when J_{ext} increases further. The three-bump steady state $\vec{\vec{S}}_{u,2}$ emerges when the four-bump steady state $\vec{\vec{S}}_{u,1}$ loses its stability with increasing J_{ext}. The stability of three-bump steady state $\vec{\vec{S}}_{u,2}$ changes from unstable to stable with increasing J_{ext}. The two-bump steady state $\vec{\vec{S}}_{u,3}$ exists only when J_{ext} is larger than a certain value. This steady state is unstable when J_{ext} is small and becomes stable as J_{ext} increases. Notably, the critical point at which the steady state changes from unstable to stable increases with the number of high bumps of the steady states. Therefore, according to the decision condition we mentioned above, a decision can be made only in the range between two vertical lines representing two critical points, at which the four-bump steady state becomes unstable and the two-bump steady state remains unstable, respectively. For two choices, the peak value of the two-equal-bump steady state and the corresponding stability change in the same way as the four-bump steady state $\vec{\vec{S}}_{u,1}$ for four-choice decision making.

We also calculated the steady states and their stability by simultaneous variation of J^+ and J_{ext} for two- and four-choice decision making (see Figure 9B). We found that parameters supporting two-choice decision making form a V-shaped domain in the parameter space of $J^+ - J_{ext}$, and the parameters supporting four-choice decision making form another V-shaped domain in the parameter space of $J^+ - J_{ext}$. The smallest J^+ is approximately

1.5 for two-choice decision making and approximately 1.511 for four-choice decision making, implying that recurrent excitation values below a certain level cannot support a decision. The parameter domains supporting two- and four-choice decision making have a large degree of overlap, indicating that our partial integro-differential system can robustly represent the multiple-choice decision task and that our results are generalizable.

4.4 Theoretical Approximation of the Reaction Time. One main goal of this study was to understand the mechanism underlying the different reaction times for different coherence levels and different numbers of choices, that is, to understand why higher coherence levels lead to quicker decisions and why it takes longer to make a decision when there are more alternatives. To achieve this aim, we investigated the local dynamics of the unstable steady state $\vec{\vec{S}}_{u,1}$ because the initial state of the system $\vec{S}_0$ lies in the vicinity of the unstable steady state $\vec{\vec{S}}_{u,1}$ and the local dynamics in the vicinity of $\vec{\vec{S}}_{u,1}$ predominantly determine the evolutionary process from $\vec{S}_0$ to the decision threshold.

As described in the local dynamics of the steady state, equation 4.4, the system exponentially departs from the steady state along the direction of the eigenvector $\vec{v}_i$ corresponding to the positive eigenvalue λ_i with a time constant τ_i defined as $1/\lambda_i$. The larger time constant implies slower evolution and longer reaction time, while the smaller time constant implies faster evolution and shorter reaction time. For two-choice decision making, there is only one positive singlet eigenvalue for $\vec{\vec{S}}_{u,1}$; thus, we define $1/\lambda_0$ as the time constant of the system, τ_0. For unbiased four-choice decision making, there is one positive triplet eigenvalue for $\vec{\vec{S}}_{u,1}$. In the case of biased decision making, however, the unstable steady state $\vec{\vec{S}}_{u,1}$ has one positive singlet of eigenvalues, λ_0, corresponding to the eigenvector $\vec{v}_0$, and one positive doublet of eigenvalues, $\lambda_{1,2}$, corresponding to the eigenvectors $\vec{v}_1$ and $\vec{v}_2$. Because evolution along the eigenvector corresponding to the singlet eigenvalue plays a major role in correct decision making, we define $1/\lambda_0$ as the time constant of the system, τ_0. Therefore, according to the local dynamics, formula 4.4, the reaction time for the correct trials, DT, can be qualitatively approximated as

$$DT \simeq \tau_0\{\ln[S_{th} - \vec{\vec{S}}_{u,1}(\theta_{mot})] - \ln c_0 - \ln \vec{v}_{0,0}(\theta_{mot})\} + 280 \text{ ms}, \tag{4.6}$$

where S_{th} is the decision threshold and 280 ms includes the latency of the motion stimulus (200 ms) and the postreaction time due to execution of the saccade (80 ms) (see equation 2.30). For simplicity, here we considered only the dimension in the motion direction because a correct decision is made when the activity of the pool preferring the motion direction exceeds the decision threshold. According to this formula, the reaction time is determined

by the time constant τ_0, the difference between the decision threshold and the value of the unstable state $\vec{\vec{S}}_{u,1}$ in the motion direction, the projection coefficient c_0 determined by the difference between the initial state S_0 and the unstable steady state, and the eigenvector $\vec{v}_{0,0}$ in the motion direction.

We calculated the time constant for two- and four-choice decision making given different coherence levels, and the results indicate that the time constant of four-choice decision making is significantly longer than that of two-choice decision making (see Figure 10A), and the mean reaction time for four-choice decisions is longer than that for two-choice decisions. However, the time constant cannot explain the fact that the mean reaction time decreases with increasing coherence levels because the time constant of the system increases slightly with the coherence levels for two choices and increases dramatically for four choices. We noticed that the coefficient c_0 varies with the coherence level as the unstable steady state $\vec{\vec{S}}_{u,1}$ varies with the coherence levels. A higher coherence level leads to a lower bump located in the motion direction in $\vec{\vec{S}}_{u,1}$ (see Figures 8D and 8E), which results in a larger difference ($\Delta\vec{S}$) and a larger projection coefficient c_0 (see Figure 10B). Therefore, the mean reaction time decreases with the projection coefficient c_0 (see formula 4.6), accounting for the observation that a higher coherence level leads to a shorter mean reaction time.

To explicitly demonstrate the overall effects of the coherence level and the number of choices on the reaction time, we calculated approximate reaction time (see formula 4.6) with the decision threshold $S_{th} = 0.77$ corresponding to the firing rate of 60 Hz. The theoretical reaction times shown in Figure 10C demonstrate a similar dependence of the decision time on the coherence level and the number of alternatives. The decision time is a monotonically decreasing function of the coherence level, and longer decision time was also observed for decisions with more alternatives. The approximated reaction time is not precisely the same as that in the simulation. The discrepancy may be due to two reasons. First, formula 4.6 is simply derived from the local dynamics in the vicinity of the unstable steady state and thus may not be suitable when the system evolves far from the unstable steady state. Second, the approximation ignores the noise, which will influence the decision time. However, the approximation is qualitatively consistent with the observations in our simulations, in monkey experiments (Churchland et al., 2008), and in the spiking network model (Wang, 2002; Wong & Wang, 2006; Furman & Wang, 2008). The approximation clearly demonstrates that the decision time depends on the time constant of the unstable steady state and the projection coefficient, a relationship that has not been previously reported in the literature.

5 Discussion

In this study, we constructed a partial integro-differential system to implement multiple-choice decision making. Our major findings include that

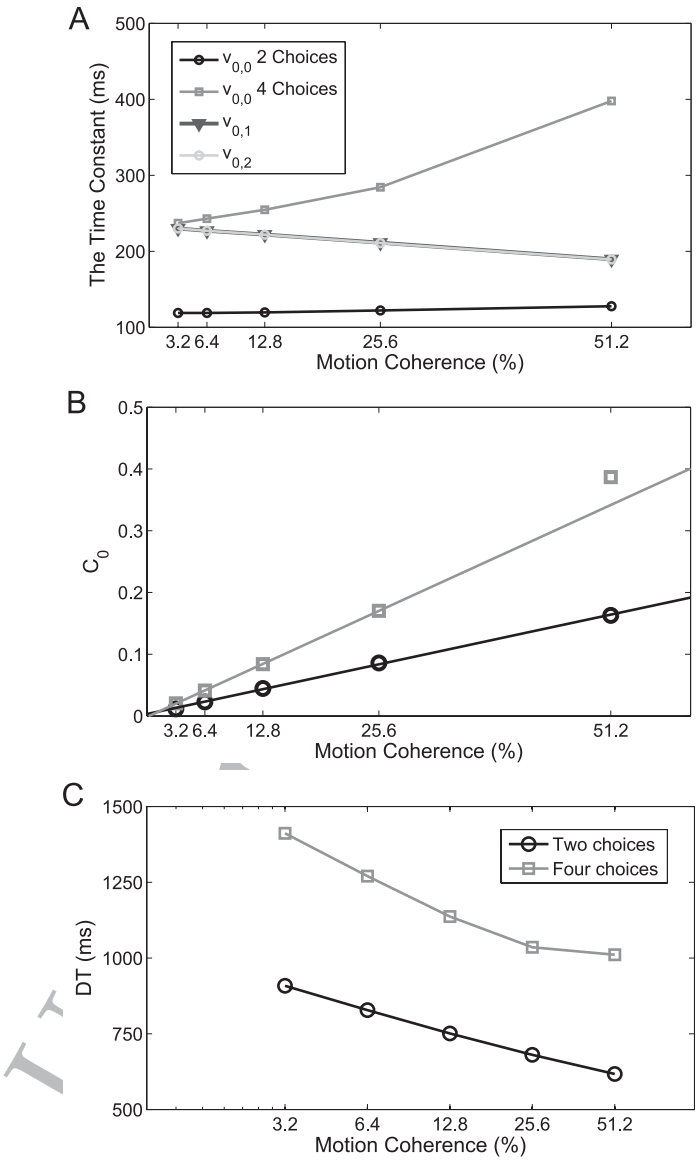

Figure 10: Approximation of the reaction time. (A) The time constants of the system are defined by the reciprocal of the largest positive eigenvalue of the unstable steady state $\vec{S}_{u,1}$. (B) The projection coefficient, c_0, for two- and four-choice decision making increases with the coherence level of the motion stimuli. (C) Approximated reaction time (see formula 4.6) for two- and four-choice decision making.

(1) the dynamics underlying two-choice decision making are different from those underlying four-choice decision making, in that the two-bump unstable steady state of the system is responsible for two-choice decision making, while four-choice decision making relies on three types of unstable steady states, and that (2) the observation that four-choice decision making requires a longer time than two-choice decision making could be explained by the time constant of their unstable steady states, but that the project coefficient, c_0, can account for quicker decisions, given higher coherence levels of the motion stimulus.

5.1 A Partial Integro-Differential System for Multiple-Choice Decisions. Many neurophysiological studies have revealed that decision making involves various brain areas, including the lateral intraparietal cortexes (LIP), the frontal eye fields (FEF), and the prefrontal cortex (Kim & Shadlen, 1999; Romo & Salinas, 2001; Gold & Shadlen, 2007). Based on the neural data resulting from the monkey experiments (Roitman & Shadlen, 2002; Shadlen & Gold, 2004; Churchland et al., 2008), biophysically plausible spiking network models including the discrete networks (Wang, 2002; Albantakis & Deco, 2009) and the continuous recurrent network (Furman & Wang, 2008) have been proposed to elucidate the neural basis of perceptual decision making in visual random-dot discrimination tasks. Here, using a mean field approach and a number of approximations (Wong & Wang, 2006), we constructed a partial integro-differential system based on the spiking network model by Furman and Wang (2008) to implement multiple-choice decision tasks. We showed that the behaviors of our model are consistent with the experimental observations (Roitman & Shadlen, 2002; Churchland et al., 2008) and the results of the models mentioned above. A stronger motion strength favors increased accuracy and quicker response, while more choices lead to reduced accuracy and longer reaction times. We also found a linear relationship between the mean and the standard deviation of the reaction time for two- and four-choice decisions, a result demonstrating that the reaction time obeys the psychophysical Weber's law (Deco & Rolls, 2006; Deco et al., 2007).

Meanwhile, the mechanisms underlying decision making have been extensively investigated. For example, Wilimzig, Schneider, and Schoner (2006) used dynamic field theory to investigate saccade decision making and concluded that instabilities are the basis of decision making. Wong and Wang (2006) used a reduced two-variable model omitting the currents mediated by the AMPA receptor and found that the system with the saddle node structure underlies two-choice decision making. Miller and Katz (2010) also achieved similar results when they studied stochastic transitions between neural states in taste-related decision making. Our partial integro-differential system, derived from a biologically plausible spiking network model, provides a unified framework for a deeper understanding of the mechanisms underlying multiple-choice decision making.

5.2 Different Dynamics Underlying Two- and Four-Choice Decision Making. The nonlinear dynamic analysis indicates that the partial integro-differential system for decision making has different dynamics given different numbers of choices. For two-choice decision making, the two-bump unstable steady state $\vec{\bar{S}}_{u1}$ is responsible for the decision. Populations, selective for different directions of targets, compete with one another in the unstable manifold connected with $\vec{\bar{S}}_{u1}$, which is consistent with previous research (Wong & Wang, 2006; Wong et al., 2007). These authors demonstrated that two-choice decision making can be implemented by a two-dimensional system with the saddle node structure, indicating that the process of two-choice decision making has one-dimensional dynamics (Ganguli et al., 2008).

In contrast, our study implies that four-choice decision making may not be a one-dimensional process. The partial integro-differential system has three types of unstable steady states $\vec{\bar{S}}_{u,1}$, $\vec{\bar{S}}_{u,2}$, $\vec{\bar{S}}_{u,3}$ for a four-choice decision system. These unstable steady states and the connecting unstable manifolds predetermine the competition among four targets and implement the four-choice decision task. The four-bump steady state $\vec{\bar{S}}_{u,1}$ connects with three unstable manifolds, resulting in competition between and within groups during the decision process. For unbiased four-choice decision making, two upward bumps of the eigenvector $\vec{v}_{0,0}$ located at 135° and 315° and the downward bumps located at 45° and 225° indicate that the network organizes into horizontal and vertical directions and the competition takes place between these two groups. The eigenvector $\vec{v}_{0,1}$ has one upward bump located at 45° and one downward bump located at 225°. This eigenvector is responsible for the competition between the leftward and rightward directions. The eigenvector $\vec{v}_{0,2}$ has one upward bump at 145° and one downward bump located at 315° and is responsible for the competition between upward and downward directions. However, for unbiased four-choice decision making, the competition between and within the groups will take place simultaneously at the same speed because the time constants of these three unstable manifolds are equal.

5.3 Projection Coefficients and Decision Processes. Our research highlights the role of the projection coefficients in the decision process. The projection coefficient c_i reflects how the the evolution of the system along the manifold tangent to the eigenvector $\vec{v}_i$ which is equivalent to the eigenfunctions of the interaction kernel in the continuous attractor model (Fung, Wong, & Wu, 2008, 2010), and represents distortions in the height and position of the bumps (not shown). Our research elucidates the influence of the projection coefficients on the decision from two aspects. First, we found that the combination of projection coefficients can predict the final choice in the decision task. Here, a four-choice decision can be used as an example. Because c_0, c_1, and c_2 are the projection coefficients of the difference $\vec{S}_0 - \vec{\bar{S}}_{u,1}$ onto the eigenvectors $\vec{v}_{0,0}$, $\vec{v}_{0,1}$, and $\vec{v}_{0,2}$, the final choice can be predicted by

the combination of c_i given unbiased four-choice decision making and the unitary perturbation of $\vec{\bar{S}}_{u,1}$ (see Table 1). For biased four-choice decision making, the target located in the motion direction will win the competition, given $c_0 > 0$, regardless of c_1 and c_2; this implies that the network will make mistakes if $c_0 < 0$. The network will choose the direction opposite to the motion if $c_1 > 0$ and the coefficient c_2 determines which of the other two targets wins the competition. In this case, the probability of making a correct choice does increase (see Table 2).

Second, our research demonstrates that project coefficients play a role in reaction time. Reaction time has been worked out based on the first passage time of the stochastic process with the variant boundary (Smith, 2000; McMillen & Holmes, 2006). The dynamic analysis has shown that the time constant of the unstable steady state of the decision system is positively related to the reaction time (Wong & Wang, 2006; Wong et al., 2007). Similarly, our research has shown that the unstable steady state of decision systems with more alternatives has a larger time constant, given an identical coherence level. However, we found that the projection coefficient c_0 plays an important role in reaction time. In the decision task, the decision is made once the system reaches the decision threshold starting from the initial state, which is close to the unstable steady state $\vec{\bar{S}}_{u,1}$. Considering that the stimuli of the targets and background noise are invariant to the coherence level of the motion, the initial state $\vec{S}_0$ is identical in the different trials. However, the unstable steady state $\vec{\bar{S}}_{u,1}$ varies with the coherence level of the motion; thus, the difference $\Delta S = \vec{S}_0 - \vec{\bar{S}}_{u,1}$ and the coefficient c_0 vary with the coherence level. Consequently, the reaction time is influenced by the coherence level of the motion. It is worth noting that the influence of the coherence level of the motion on the reaction time through the projection coefficient of the difference between the initial state and the unstable steady state on the eigenvectors has not been previously reported.

5.4 The Discrete Recurrent Network and the Continuous Recurrent Network. In recent years, two types of biophysically plausible spiking network models have been proposed to investigate perceptual decision making in the visual random-dot discrimination task. One type is the discrete recurrent attractor model that represents the choice alternatives by several separate and homogeneous neural populations (Wang, 2002; Albantakis & Deco, 2009) and the other is the continuous recurrent attractor model that represents a continuum of directions of motion (Furman & Wang, 2008; Liu & Wang, 2008). It is worthwhile to compare the two types of the models. First, these models have been extensively used to investigate higher cognitive functions in addition to decision making. The discrete model has been used to investigate working memory with discrete item and hysteresis (Brunel & Wang, 2001; Amit, Bernacchia, & Yakovlev, 2003; You, Meng, Huan, & Wang, 2011). The continuous model also has been used to characterize

visual working memory (Compte et al., 2000; Edin et al., 2009; Wei, Wang, & Wang, 2012). Second, these two types of models share similar dynamics in decision making. For multiple-choice decision making, a spiking network with four discrete neuron pools has been used to investigate four-choice decision making (Albantakis & Deco, 2009). Mean field analysis showed three types of states of the model: the decision state, the spontaneous state, and mixed states. The existence and stability of these states determine whether decisions can be made. In our continuous model, there are stable states (one-bump states), unstable states with two or four bumps, and other unstable states. The local dynamics of the unstable steady state $\vec{S}_{u,1}$ indicate how the continuous model can illustrate the decision process. Third, the dynamic structure, including the stable and unstable steady states, depends on the parameters of the model. We showed the dependence of the steady states and the corresponding stability on the parameter configurations (the external input strength and the strength of the iso-directional connections), indicating a broad parameter range simultaneously supporting two- and four-choice decision making in our continuous model. Finally, although the continuous model seems more complex than the discrete model, it is much easier to alter the number of options in the decision-making task using a continuous model.

Appendix: Symbols, Variables and Parameters in the Model

	Populations
E, I	Pyramidal cells (E), interneurons (I)
θ	Pyramidal cells: tuned by their preferred directions, which uniformly cover all directions along a circle; interneurons: nonselective
	Neurons
$r_{E,I}$	Instantaneous firing rate of pyramidal cells and interneurons, respectively
τ_r	Time constant of the population firing rate
$c_{E,I}, I_{E,I}, g_{E,I}$	Parameters of the activation function $\phi(I_{syn})$ of the excitatory and inhibitory populations
	Synapses and Synaptic Currents
$AMPAR$	α-amino-3-hydroxy-5-methyl-4-isoxazolepropionic acid receptors
$NMDAR$	N-methyl-D-aspartate receptors
$GABAR$	Gamma-aminobutyric acid receptors
$S_{AMPA}, S_{NMDA}(S), S_{GABA}$	Gating variables of $AMPAR$, $NMDAR$ and $GABAR$, respectively
$\tau_{AMPA}, \tau_{NMDA}(\tau_s), \tau_{GABA}$	Time constants of their gating variables
$I_{E,syn}, I_{I,syn}$	Total synaptic currents to pyramidal cells and interneurons, respectively
$I_R^{T_1 \to T_2}$	Synaptic currents from T_1 to T_2 mediated by R receptors, $R \in \{AMPA, NMDA, GABA\}$, $T_1 \in \{E, I, Ext, Back\}$, $T_2 \in \{E, I\}$

J_{R,T_2T_1}	Contribution coefficients of the gating variables of R receptors to synaptic currents of pyramidal cells and interneurons, $T_1, T_2 \in \{E, I\}$
J_{EE}	Effective *NMDAR*-mediated synaptic conductance in the partial integro-differential system
J_{EIE}	Effective synaptic conductance of mutual inhibition in the partial integro-differential system
$W(\Delta\theta)$	Overall synaptic conductance of mutual interactions of excitatory pools in the partial integro-differential system
	Connectivity
$\omega(\Delta\theta)$	The connection strength between pyramidal cells is a gaussian function of the difference between their preferred directions ($\Delta\theta$)
$\omega_{E\leftrightarrow I}, \omega_{I\leftrightarrow I}$	Connections to and from interneurons
J^-, J^+, σ_w	Strength of the cross- and iso-directional connections and connection width of pyramidal cells
	Task-Related External Stimuli and Noise Input
I^{Tar}_{AMPA}	Target input
n_{tar}	Number of targets
θ_{tar}	Direction of the targets. Two choices: 90°, 270°; four choices: 45°, 135°, 225°, 315°
I^{Mot}_{AMPA}	Motion stimulus
θ_{mot}	Random-dot motion direction
c'	Coherence level, percentage of coherently moving dots
J_{ext}	External input strength
$I_{control}$	Top-down control signal
$I_{inhibitory}$	Inhibitory input
I_{noise}	Time-varying noise input
σ^2_{noise}	Variance of the time-varying noise input

Acknowledgments

We thank Si Wu and KongFatt Wong for discussions. This work was supported by NSFC under grants 60974075, 31271169, and 91130702 and the Fundamental Research Funds for the Central Universities. A.Y. also thanks the support from the China Scholarship Council.

References

Abbott, L. F., & Chance, E. S. (2005). Drivers and modulators from push-pull and balanced synaptic input. *Progress in Brain Research*, *149*, 147–155.

Albantakis, L., & Deco, G. (2009). The encoding of alternatives in multiple-choice decision making. *Proc. Nat. Acad. Sci. USA*, *106*, 10308–10313.

Amit, D. J., Bernacchia, A., & Yakovlev, V. (2003). Multiple-object working memory: A model for behavioral performance. *Cerebral Cortex*, *13*, 435–443.

Bogacz, R., Usher, M., Zhang, J., & McClelland, J. L. (2007). Extending a biologically inspired model of choice: Multi-alternatives, nonlinearity and value-based multidimensional choice. *Phil. Trans. R. Soc. B*, *362*, 1655–1670.

Bollimunta, A., Totten, D., & Ditterich, J. (2012). Neural dynamics of choice: Single-trial analysis of decision-related activity in parietal cortex. *Journal of Neuroscience*, *32*(37), 12684–12701.

Brunel, N., & Wang, X-J. (2001). Effects of neuromodulation in a cortical network model of object working memory dominated by recurrent inhibition. *J. Comput. Neurosci.*, *11*, 63–85.

Churchland, A. K., Kiani, R., & Shadlen, M. N. (2008). Decision-making with multiple alternatives. *Nature Neuroscience*, *11*, 693–702.

Compte, A., Brunel, N., Goldman-Rakic, P. S., & Wang, X.-J. (2000). Synaptic mechanisms and network dynamics underlying visuospatial working memory in a cortical network model. *Cerebral Cortex*, *10*, 910–923.

Constantinidis, C., & Steinmetz, M. (1996). Neuronal activity in posterior parietal area 7a during the delay periods of a spatial memory task. *Journal of Neurophysiology*, *76*, 1352–1355.

Constantinidis, C., Franowicz, M. N., & Goldman-Rakic, P. S. (2001). Coding specificity in cortical microcircuits: A multiple-electrode analysis of primate prefrontal cortex. *Journal of Neuroscience*, *21*, 3646–3655.

Deco, G., & Rolls, E. (2006). Decision-making and Weber's law: A neurophysiological model. *Eur. J. Neurosci.*, *24*, 901–916.

Deco, G., Scarano, L., & Soto-Faraco, S. (2007). Weber's law in decision making: Integrating behavioral data in humans with a neurophysiological model. *Journal of Neuroscience*, *27*, 11192–11200.

Destexhe, A., Rudolph, M., Fellous, J. M., & Sejnowski, T. J. (2001). Fluctuating synaptic conductances recreate in vivo–like activity in neocortical neurons. *Neuroscience*, *107*, 13–24.

Ditterich, J. (2010). A comparison between mechanisms of multi-alternative perceptual decision making: Ability to explain human behavior, predictions for neurophysiology, and relationship with decision theory. *Frontiers in Neuroscience*, *4*, 184.

Edin, F., Klingberg, T., Johansson, P., McNab, F., Tegner, J., & Compte, A. (2009). Mechanism for top-down control of working memory capacity. *Proc. Nat. Acad. Sci. USA*, *106*, 6802–6807.

Furman, M., & Wang, X.-J. (2008). Similarity effect and optimal control of multiple-choice decision making. *Neuron*, *60*, 1153–1168.

Fung, C. A., Wong, K. Y., & Wu, S. (2008). Dynamics of neural networks with continous attractors. *Europhys. Lett.*, *84*, 18002.

Fung, C. C., Wong, K. Y., & Wu, S. (2010). A moving bump in a continuous manifold: A comprehensive study of the tracking dynamics of continuous attractor neural networks. *Neural Computation*, *22*, 752–792.

Ganguli, S., Bisley, J. W., Roitman, J. D., Shadlen, M. N., Goldberg, M. E., & Miller, K. D. (2008). One-dimensional dynamics of attention and decision making in LIP. *Neuron*, *58*, 15–25.

Gillespie, D. T. (1996). The mathematics of Brownian motion and Johnson noise. *American Journal of Physics*, *64*, 225–240.

Gold, J., & Shadlen, M. N. (2007). The neural basis of decision making. *Annu. Rev. Neurosci.*, *30*, 535–574.

Kable, J. W., & Glimcher, P. W. (2009). The neurobiology of decision: Consensus and controversy. *Neuron.*, *63*, 733–745.

Kim, J. N., & Shadlen, M. N. (1999). Neural correlates of a decision in the dorsolateral prefrontal cortex of the macaque. *Nature Neuroscience*, *2*, 176–185.

Liu, F., & Wang, X.-J. (2008). A common cortical circuit mechanism for perceptual categorical discrimination and veridical judgment. *PLoS Comput Biol*, *4*, e1000253.

McMillen, T., & Holmes, P. (2006). The dynamics of choice among multiple alternatives. *Journal of Mathematical Psychology*, *50*, 30–57.

Miller, P., & Katz, D. B. (2010). Stochastic transitions between neural states in taste processing and decision-making. *Journal of Neuroscience*, *30*, 2559–2570.

Niwa, M., & Ditterich, J. (2008). Perceptual decisions between multiple directions of visual motion. *Journal of Neuroscience*, *28*, 4435–4445.

Press, W. H., Teukolsky, S. A., Vetterling, W. T., & Flannery, B. P. (1992). *Numerical recipes in C: The art of scientific computing* (2nd ed.). Cambridge: Cambridge University Press.

Roitman, J. D., & Shadlen, M. N. (2002). Response of neurons in the lateral intraparietal area during a combined visual discrimination reaction time task. *Journal of Neuroscience*, *22*, 9475–9489.

Romo, R., & Salinas, E. (2001). Touch and go: Decision-making mechanisms in somatosensation. *Annu. Rev. Neurosci.*, *24*, 107–137.

Shadlen, M. N., & Gold, J. (2004). The neurophysiology of decision-making as a window on cognition. In M. S. Gazzaniga (Ed.), *The cognitive neurosciences* (3rd ed.). Cambridge, MA: MIT Press.

Smith, P. L. (2000). Stochastic dynamic models of response time and accuracy: A foundational primer. *Journal of Mathematical Psychology*, *44*, 408–463.

Strogatz, S. (2001). *Nonlinear dynamics and chaos: With applications to physics, biology, chemistry, and engineering*. Boulder, CO: Westview Press.

Wang, X.-J. (2002). Probabilistic decision making by slow reverberation in cortical circuits. *Neuron*, *36*, 955–968.

Wang, X.-J. (2008). Decision making in recurrent neuronal circuits. *Neuron*, *60*, 215–234.

Wei, Z., Wang, X.-J., & Wang, D.-H. (2012). From distributed resources to limited slots in multiple-item working memory: A spiking network model with normalization. *Journal of Neuroscience*, *32*, 11228–11240.

Wilson, H., & Cowan, J. (1972). Excitatory and inhibitory interactions in localized populations of model neurons. *Biophysical Journal*, *12*, 1–24.

Wilson, H., & Cowan, J. (1973). A mathematical theory of the functional dynamics of cortical and thalamic nervous tissue. *Kybernetik*, *13*, 55–80.

Wilimzig, C., Schneider, S., & Schoner, G. (2006). The time course of saccadic decision making: Dynamic field theory. *Neural Networks*, *19*, 1059–1074.

Wong, K.-F., & Wang, X.-J. (2006). A recurrent network mechanism of time integration in perceptual decisions. *Journal of Neuroscience*, *26*, 1314–1328.

Wong, K.-F., Huk, A. C., Shadlen, M. N., & Wang, X.-J. (2007). Neural circuit dynamics underlying accumulation of time-varying evidence during perceptual decision making. *Neuroscience*, *1*, 1–11.

You, H., Meng, Y., Huan, D., & Wang, D.-H. (2011). The neural dynamics for hysteresis in visual perception. *Neurocomputing*, *74*, 3502–3508.

Received July 3, 2012; accepted January 31, 2013.